

# Contents

<b>1</b>	<b>Introduction</b>	<b>3</b>
<b>2</b>	<b>Medical Background</b>	<b>5</b>
2.1	Anatomy of the central nervous system . . . . .	5
2.2	The Spinal Cord . . . . .	5
2.3	The Chiari malformation . . . . .	6
2.3.1	Syringomyelia . . . . .	6
<b>3</b>	<b>Mathematical background</b>	<b>9</b>
3.1	Fluid flow . . . . .	9
3.1.1	Reynolds Transport Theorem . . . . .	10
3.1.2	Conservation of mass and momentum . . . . .	11
3.1.3	Incompressible Newtonian fluids . . . . .	13
3.2	Navier-Stokes equations for incompressible flow . . . . .	13
3.2.1	Boundary conditions . . . . .	14
3.3	Linear Elasticity . . . . .	15
3.4	Linear Poroelasticity . . . . .	15
3.4.1	Fluid flow through a porous media . . . . .	15
3.4.2	Biot's equations . . . . .	17
3.5	Descriptions of Motion . . . . .	17
3.5.1	Lagrangian and Eulerian descriptions of motion . . . . .	17
3.5.2	The Arbitrary Eulerian Lagrangian description . . . . .	19
3.6	Balance equations in the ALE framework . . . . .	22
3.6.1	Mesh updating . . . . .	22
3.7	Fluid Structure Interaction . . . . .	23
<b>4</b>	<b>Numerical Methods</b>	<b>25</b>
4.1	The Finite Element Method . . . . .	25
4.1.1	Variational formulation . . . . .	25
4.1.2	Finite elements . . . . .	27
4.1.3	Implementation in FEniCS . . . . .	28
4.2	A benchmark FSI-problem . . . . .	30
4.2.1	Domain, Initial- and boundary conditions . . . . .	31
4.2.2	CFD tests . . . . .	32
4.2.3	CSM tests . . . . .	33
4.2.4	FSI tests . . . . .	36
4.3	Fluid Structure Interaction using the Finite Element method . . . . .	39
4.3.1	Temporal discretization . . . . .	39

4.3.2	Spatial discretization . . . . .	39
4.3.3	A discussion on functionspaces . . . . .	40
4.3.4	Treatment of boundary conditions . . . . .	42
4.3.5	FSI in FEniCS . . . . .	43
4.4	A Discontinuous Galerkin method . . . . .	47
4.4.1	Stokes flow . . . . .	48
4.5	Womersley Flow . . . . .	49
4.5.1	A penalty method for the boundary conditions . . . . .	52
<b>5</b>	<b>Material parameters</b>	<b>55</b>
<b>6</b>	<b>Simulating interaction between CSF and the Spinal Cord</b>	<b>57</b>
6.1	Overview of previous studies . . . . .	57
6.1.1	Pressure measurements in patients with syringomelia . . . . .	58
6.2	Assessment of CSF velocities before and after decompression surgery	59
6.3	Linear Results . . . . .	60
6.4	Nonlinear Results . . . . .	62

# Chapter 1

## Introduction

The Cerebrospinal Fluid (CSF) surrounds the brain and acts as a protection to the brain inside the skull. As a result of the cardiac cycle the CSF will flow up and down the subarachnoid space (SAS) surrounding the spinal cord. The Chiari malformation is a displacement of the cerebellar tonsils that partially blocks CSF flow entering the SAS around the spinal cord. This causes abnormal CSF flows which sometimes results in in a syringomyelia inside the spinal cord filled with fluid. Treatment may include surgery to remove parts of the bones of the skull to relieve pressure. Studies have shown that the syrinx gradually vanishes after surgery. The mechanisms behind this are not yet fully understood. Many researchers have suggested Computational Fluid Dynamics (CFD) to give useful insight, as experiments are very difficult and expensive.

This thesis is a continuation of the work at Simula Research Laboratory and the University of Oslo regarding abnormal CSF flow related to the Chiari I malformation. Previous master and PhD studies at the University of Oslo includes the works of Støverud, Kylstad and Drosdal. [1] [2] [3].



## Chapter 2

# Medical Background

In this chapter, a short description of the problem setting from a medical point of view is given. If not specified, the information given below is based on the textbook "Human Anatomy and Physiology", by Van Wynsberghe, Noback, and Carola [4]

### 2.1 Anatomy of the central nervous system

The human nervous system consists of peripheral nervous system, and the central nervous system (CNS). The former consists of spinal and cranial nerves and sensory receptor organs while the latter consists of two parts: the brain and the spinal cord. The CNS receives and processes information from all parts of the body. Consequently, studies on the CNS are crucial for our understanding of the human anatomy.

### 2.2 The Spinal Cord

The spinal cord carries information between the body and the brain and is divided into four or five regions from top to bottom: Cervical (C), thoracic (T), lumbar (L) and sacral (S) in addition to the coccygeal part at the very bottom. The upper end of the spinal cord is continuous with the lowermost part of the brain, while the lower part tapers at the filum terminale, which attaches to the coccyx, known as the tailbone. Along the cord, there are 31 pairs of nerves exiting the cord: 8 in the cervical region, 12 in the thoracic region, 5 in the lumbar region, 5 in the sacral region and one in the coccygeal region. The first four segments of the cord are given names C1-C8, T1-T12, L1-L5, S1-S5. The tissue within the spinal cord consists of nervous tissue in form of white and grey matter which differs in both structure and function. In the center of the spinal cord, lies a tiny central spinal canal where CSF can flow. This channel closes off with age. Surrounding the central canal lies the gray matter in an H-shape, similar to a butterfly. The rest consists of white matter, and the ratio between white and gray matter differs along the spinal cord.

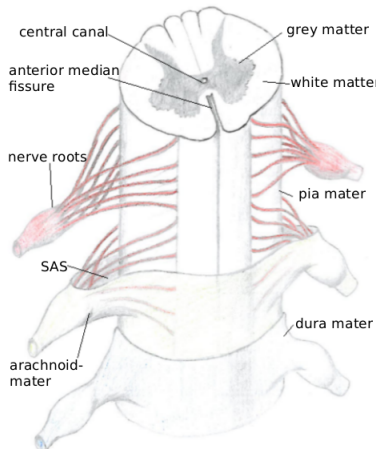


Figure 2.1: Schematic figure of the spinal cord. The pia mater surrounds the spinal cord, and between the pia mater and dura mater lies the subarachnoid space where CSF flows

There are three layers covering the brain and spinal cord known as meninges. The innermost layer surrounds the spinal cord and is known as the *pia mater*. The pia contains blood vessels that nourish the spinal cord. The middle layer, the *arachnoid* runs caudally extending almost all the way down the spinal cord. At the S2 vertebral level, the arachnoid joins the filum terminale. The outermost layer of the meninges protecting the spinal cord is known as the *dura mater* and is a though fibrous membrane.

## 2.3 The Chiari malformation

The Chiari malformation, also known as Arnold-Chiari Malformation is a neurological condition where a displacement of the cerebellum, or more presice the cerebellar tonsils, down through the foramen magnum occur. The condition is classified into four stages I-IV where IV is the most severe. In a Chiari patient, the cerebellar tonsils obstructs the CSF flow (see figure 2.2) and even Chiari I patients have shown to have greater CSF velocities and a more complex flow pattern than healty subjects. [5] These patients could also experience severe headache, dizziness, tinnitus and muscle weakness. As the cerebellum is part of the brain that controls balance, loss of coordination have also been reported.

### 2.3.1 Syringomelia

In some cases, Chiari patients develops a fluid cavity, known as a syrinx within the spinal cord. Some of the symptoms are similar to the Chiari patients in general, but include muscle and back pain, weakness, numbness and inabilities

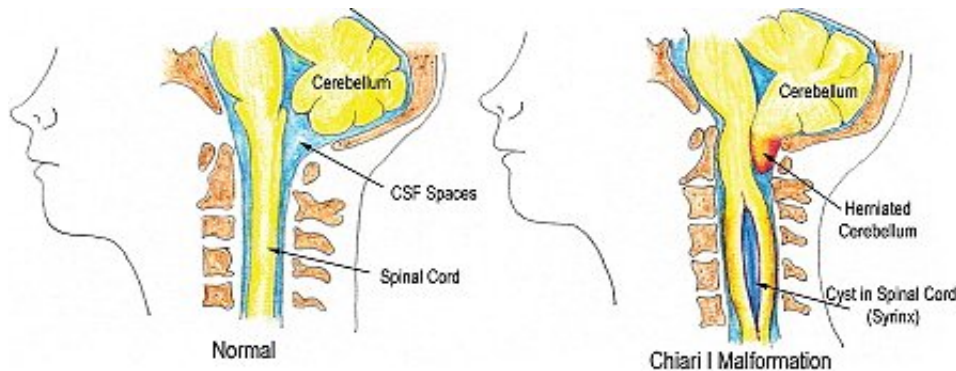


Figure 2.2: The Chiari malformation. Healthy subject to the left and a downward displacement of the cerebellar tonsils on the right

to feel temperature changes. Many theories on the pathogenesis of syringomelia have been proposed, but the details are not yet fully understood. In patients diagnosed with Chiari I, about 2/3 develops syrinxes within the spinal cord tissue. Thus, not all Chiari patients have syringomelia and in addition patients with syringomelia does not necessarily have the Chiari malformation. Thompson et al. have in a recent study suggested the anatomy of the cervical (upper part) spinal canal plays a role in the formation of syrinxes. [6] The study showed that Chiari patients with syringomelia had greater *C4-C7*-tapering of the cervical spinal canal, but no significant difference on *C1-C4*-tapering. Tapering is the narrowing of the spinal canal in the downwards, or caudal direction.

Most researchers seem to agree on the fact that altered CSF dynamics is associated with the formation of the syrinx.



## Chapter 3

# Mathematical background

The flow of CSF around the spinal cord requires equations for fluid flow to be coupled with equations for elasticity or in the optimal case, poroelasticity. The underlying concepts of these kinds of problems were originally developed somewhat independently within petroleum engineering, geomechanics and hydrogeology. The equations will first be presented separately. Later in the chapter, coupling conditions will be discussed. Several quantities will be discussed and we try to use a consistent notation for each quantity throughout the study.

This chapter intends to give a short description of the mathematical theory behind modeling of CSF. The equations are first introduced by assuming a fixed set of coordinates. Later, the two fundamental descriptions of motion are discussed.

In this thesis we use the following notation for the physical quantities:

**v** - Velocity of the material. In the fluid, **v** represents fluid velocity, and in the solid **v** denotes the velocity of the solid.

**U** - Total displacement of the solid. In the fluid, this quantity represents the total mesh displacement.

**p** - Pressure in the fluid. In the case of elasticity, the same pressure does not exist in the solid, but in the case of an (almost) incompressible solid, an extra equation involving **p** can be set up in the solid as well.

**w** - Domain velocity, (i.e, all material points within the domain moves with velocity **w**). In the solid, the domain changes with the velocity of the solid, **v**, so in the solid we have **v** = **w** which will not necessarily hold in the fluid.

Subscripts f and s are used to denote fluid and solid quantities, respectively

### 3.1 Fluid flow

The most fundamental equations in fluid flow are conservation laws. These equations are based on classical mechanics and states conservation of mass,

momentum and energy. In the literature, these are often referred to as balance equations.

### 3.1.1 Reynolds Transport Theorem

The famous engineer and scientist Osbourne Reynold stated the general conservation law the following way [7]:

Any change whatsoever in the quantity of any entity within a closed surface can only be effected in one or other of two distinct ways:

1. it may be effected by the production or destruction of the entity within the surface, or
2. by the passage of the entity across the surface.

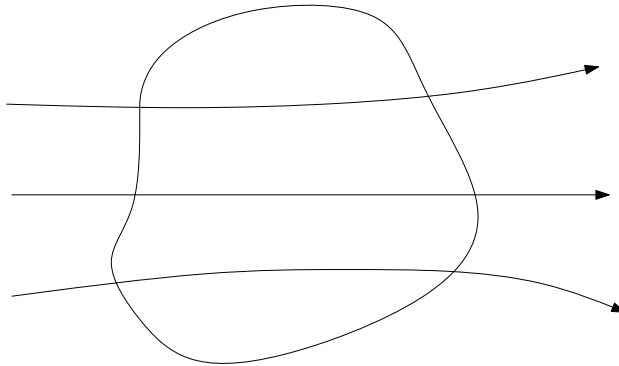


Figure 3.1: Fixed control volume with flow as indicated by streamlines

It should be noted that the transport theorem can be approached in two different ways. One for a fixed set of spatial coordinates, a fixed control volume, where fluid can enter and exit the boundaries of the defined body. The other approach has a control volume consisting of the same material particles at all times. Therefore the body has to follow the flow, and no fluid will cross the boundary. In this approach, one has to take into account the movement of the boundary of the body and the fact that the body can change its volume. More on descriptions of motion is described in section 3.5

Now, consider a fixed control volume,  $V_0$  and some fluid property  $Q(\mathbf{x}, t)$ . The rate of change of  $Q$  within the control volume can be written

$$\frac{d}{dt} \int_{V_0} Q(\mathbf{x}, t) dV$$

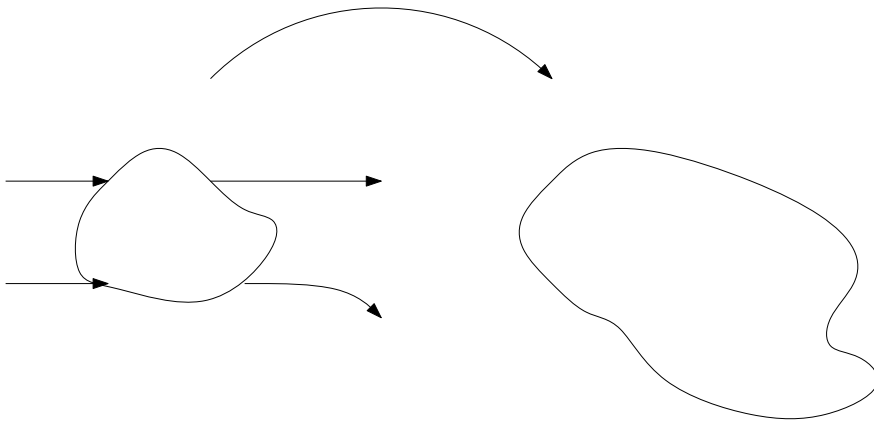


Figure 3.2: A moving control volume, consisting of the same fluid particles at time  $t$  (left) and time  $t + \Delta t$  (right)

The net change of  $Q$  must be equal the rate of change in  $Q$  within the control volume plus the net rate of mass flow out of the volume. In other words:

$$\frac{d}{dt} \int_{V_0} Q(\mathbf{x}, t) dV = \int_{V_0} \frac{\partial Q(\mathbf{x}, t)}{\partial t} dV + \int_{S_0} Q(\mathbf{x}, t) \mathbf{v} \cdot \mathbf{n} dS$$

Here,  $\mathbf{v}$  denotes fluid velocity, and  $\mathbf{n}$  denotes the outward pointing unit-normal, i.e  $\mathbf{n}$  points *out* of the fluid. This equation is known as the Reynold's transport theorem. The right hand side could be rewritten by using Gauss' theorem on the last term.

$$\frac{d}{dt} \int_{V_0} Q(\mathbf{x}, t) dV = \int_{V_0} \left[ \frac{\partial Q(\mathbf{x}, t)}{\partial t} + \nabla \cdot (Q(\mathbf{x}, t) \mathbf{v}) \right] dV \quad (3.1)$$

where

$$\nabla = \mathbf{i}_j \frac{\partial}{\partial x_j}$$

### 3.1.2 Conservation of mass and momentum

Choose  $Q(\mathbf{x}, t) = \rho$ , where  $\rho$  is fluid density. Conservation of mass means that

$$\frac{d}{dt} \int_{V_0} \rho dV = 0$$

And by using the transport theorem (3.1)

$$\int_{V_0} \left[ \frac{\partial \rho}{\partial t} + \nabla \cdot (\rho \mathbf{v}) \right] dV = 0$$

This should hold for any volume  $V_0$ , hence the integrand has to be zero. If there existed a point where the integrand were not zero, the control volume could be

an arbitrary small enclosed sphere around this point, and the volume integral would not be zero. Therefore,

$$\frac{\partial \rho}{\partial t} + \nabla \cdot (\rho \mathbf{v}) = 0 \quad (3.2)$$

(3.2) is known as the continuity equation and states conservation of mass.

To derive a similar property for the momentum, Newtons second law of motion can be used. The net change of momentum must be equal to the applied forces to the system. The forces can be divided into volume forces, acting on the entire control volume, and forces acting only on the control surface. The forces acting on the surface can be written  $\sigma_f \cdot \mathbf{n}$ , where  $\sigma_f = \sigma_f(\mathbf{v}, p)$  is the tensor denoting the total stress.

This can be written

$$\frac{d}{dt} \int_{V_0} \rho \mathbf{v}(\mathbf{x}, t) dV = \int_{\partial V_0} \sigma_f \cdot \mathbf{n} dS + \int_{V_0} \mathbf{F}_v dV$$

By using the Transport Theorem on the left hand side and with Gauss' theorem on the right hand side we end up with

$$\int_{V_0} \left[ \frac{\partial \rho \mathbf{v}}{\partial t} + \nabla \cdot (\rho \mathbf{v} \mathbf{v}) - \nabla \cdot \sigma_f - \mathbf{F}_v \right] dV = 0$$

With the same argument as before the integrand has to be zero, and with some rearrangement:

$$\frac{\partial \rho \mathbf{v}}{\partial t} + \nabla \cdot (\rho \mathbf{v} \mathbf{v}) = \nabla \cdot \sigma_f + \mathbf{F}_v \quad (3.3)$$

The left hand side can be rewritten to

$$\rho \frac{\partial \mathbf{v}}{\partial t} + \mathbf{v} \frac{\partial \rho}{\partial t} + \mathbf{v} \mathbf{v} \cdot \nabla \rho + \rho \mathbf{v} \cdot \nabla \mathbf{v} + \mathbf{v} \rho \cdot \nabla \mathbf{v} = \rho \left( \frac{\partial \mathbf{v}}{\partial t} + (\mathbf{v} \cdot \nabla) \mathbf{v} \right) + \left( \frac{\partial \rho}{\partial t} + \nabla \cdot (\mathbf{v} \rho) \right)$$

And the last term is zero due to mass conservation. Equation (3.3) can then be written

$$\rho \left( \frac{\partial \mathbf{v}}{\partial t} + (\mathbf{v} \cdot \nabla) \mathbf{v} \right) = \nabla \cdot \sigma_f + \mathbf{F}_v \quad (3.4)$$

The stress tensor,  $\sigma_f$ , depends on fluid properties and will be defined in the next subsection. Equation (3.4) is known as the momentum equation as it states conservation of momentum.

The energy equation for an incompressible flow is given by

$$\rho c_p \frac{\partial T}{\partial t} + \mathbf{v} \cdot \nabla T = k \nabla^2 T + \Phi$$

Where  $c_p$  is the heat capacity and  $\Phi$  is the dissipation function. When  $\rho$  and  $\mu$  is constant, the other two balance equations, (3.2) and (3.4), are uncoupled from the energy equation, and thus ignored from the set of equations.

### 3.1.3 Incompressible Newtonian fluids

In this text we will only consider incompressible fluid flow for a Newtonian fluid. The assumption of a Newtonian fluid requires the viscous stresses to be linear functions of the components of the strain-rate tensor, denoted by  $\epsilon$ . These assumptions were first made by Stokes in 1845. Stokes' assumptions have later proven to be quite accurate for all gases and most common fluids. Stokes' three postulates regarding the deformation laws are: [8]

1. The fluid is continuous, and its stress tensor,  $\sigma_{f_{ij}}$  is at most a linear function of the strain rates,  $\epsilon_{ij}$
2. The fluid is isotropic, i.e., its properties are independent of direction, and therefore the deformation law is independent of the coordinate axes in which it is expressed.
3. When the strain rates are zero, the deformation law must reduce to the hydrostatic pressure condition,  $\sigma_{f_{ij}} = -p\delta_{ij}$ , where  $\delta_{ij}$  is the Kroenecker delta function.

From the first and third condition the following assumption can be made

$$\sigma_{f_{ij}} = -p\delta_{ij} + M_{ijkl}\epsilon_{kl} \quad (3.5)$$

It can be shown that symmetry of  $\sigma_f$  and  $\epsilon$  also requires symmetry of  $M$ . This assumption reduces the number of coefficients in (3.5) from 36 to 21. If Stokes' second condition is also taken into account and the fluid properties are identical in each direction the number of coefficients are further reduced to 2. These simplifications allow us to denote the stress tensor the following way:

$$\sigma_{f_{ij}} = -p\delta_{ij} + 2\mu\epsilon_{ij} + \lambda\nabla \cdot \mathbf{v} \quad (3.6)$$

where  $\epsilon_{i,j} = \frac{1}{2}(\frac{\partial u_i}{\partial x_j} + \frac{\partial u_j}{\partial x_i})$ ,  $p$  is the fluid pressure and  $\mu$  and  $\lambda$  are known as Lame's constants. In the present study we only consider incompressible flow where  $\rho$  is constant. From the continuity equation (3.2), this implies  $\nabla \cdot \mathbf{v} = 0$  and the last term in (3.6) vanishes. Furthermore,

$$\nabla \cdot \epsilon = \frac{\partial}{\partial x_j}(\frac{\partial u_j}{\partial x_i} + \frac{\partial u_i}{\partial x_j})\mathbf{i}_i = (\frac{\partial}{\partial x_i}\frac{\partial u_j}{\partial x_j} + \frac{\partial u_i}{\partial x_j}\frac{\partial u_j}{\partial x_i})\mathbf{i}_i = \frac{\partial u_i}{\partial x_j}\frac{\partial u_j}{\partial x_i}\mathbf{i}_i$$

Which simplifies the representation of  $\nabla \cdot \sigma_f$  in (3.4) for an incompressible fluid

## 3.2 Navier-Stokes equations for incompressible flow

The system (3.2),(3.4) are commonly referred to as the Navier-Stokes equations written in *divergence form*, where the Cauchy stress tensor,  $\sigma$  is explicitly included in the momentum equation and contributes to the momentum through its divergence. However, in the case of Newtonian incompressible fluids, the simplifications described in the previous section allows us to write the system of equations in *laplace form*

$$\rho(\frac{\partial \mathbf{v}}{\partial t} + (\mathbf{v} \cdot \nabla)\mathbf{v}) = -\nabla p + \mu\nabla^2\mathbf{v} + \mathbf{F}_v$$

$$\nabla \cdot \mathbf{v} = 0$$

The parameters  $\rho$  and  $\mu$  describe fluid density and dynamic viscosity. Often, the momentum equation is written in terms of the kinematic viscosity  $\nu = \frac{\mu}{\rho}$  by dividing the momentum equation with  $\rho$ .

It should be noted that the two formulations of the momentum equation are equivalent in their original form. In textbooks, see e.g. [9, 8, 10], the Laplace form is usually the form first presented as the Navier-Stokes equations probably because it is the simplest form explicitly including the two unknowns  $\mathbf{v}$  and  $p$ .

The Navier-Stokes equations are coupled and non-linear and can generally not be solved analytically. However, numerous analytical solutions have been carried out for different specific problems, and a good overview is given by White [8, pp. 97-164]. (Further references are also given in this textbook for the interested reader) These problems are often very simple and idealized. Hence, numerical solutions are a necessity to obtain useful solutions to real-life problems. Such methods will be discussed in chapter 4.

### 3.2.1 Boundary conditions

Before the equations can be solved, appropriate boundary conditions need to be imposed on all boundaries of the domain. For a specific fluid occupying a domain, the treatment of boundary conditions is what distinguishes different flow patterns as the governing equations inside the domain stay exactly the same.

A fluid generally moves around between solid boundaries,  $\Gamma_D$  and boundaries known as traction boundaries  $\Gamma_N$ .

On  $\Gamma_D$  e.g. the interface between a fluid and a solid wall, the fluid velocity must equal the wall velocity in all directions, often known as the no-slip boundary condition. For instance at a rigid wall, the boundary condition will be  $\mathbf{v} = 0$  on  $\Gamma_D$ , or in general

$$\mathbf{v} = \mathbf{v}_0 \quad \text{on } \Gamma_D$$

On  $\Gamma_N$  external forces on the system must be imposed. At surfaces where arbitrary forces  $\bar{\mathbf{F}}$  are acting, the fluid stress on the surface must equal these external forces. This can be written

$$\sigma \cdot \mathbf{n} = \bar{\mathbf{F}} \quad \text{on } \Gamma_N$$

Where  $\mathbf{n}$  is the outward normal unit vector.

This is also the case of a free surface, except the shear forces are negligible and that only external pressures are applied. This yields

$$\sigma \cdot \mathbf{n} = -p_0 \mathbf{n} \quad \text{on } \Gamma_N$$

where  $p_0$  is a known external pressure, for instance atmospheric pressure at the ocean surface.

A third option is the so called pseudo-traction boundary condition, where we set

$$\mu \frac{\partial \mathbf{v}}{\partial n} - p \mathbf{n} = -p_0 \mathbf{n}$$

where  $p_0$  is some prescribed pressure. This boundary condition is often associated with the laplace form of the Navier-Stokes equation as it is what naturally appears on the boundary when integrating the weak form of the Laplace term by parts.

### 3.3 Linear Elasticity

Linear elasticity is an approximation used for small deformations for elastic solids. As a rule of thumb the approximation of linear elasticity is usually valid for deformations up to 10% relative to the solid. The stress tensor for a linear elastic medium is very similar to (3.6) describing an incompressible Newtonian fluid except there is no fluid pressure, and the stress is related to the total displacement  $\mathbf{U}$  rather than the velocity  $\mathbf{v}$ . The stress tensor for such a material reads:  $\sigma_s = 2\mu\epsilon(\mathbf{U}) + \lambda\text{tr}(\mathbf{U})$ , where  $\epsilon$  is as described earlier.

$$\rho \frac{\partial^2 \mathbf{U}}{\partial t^2} = \nabla \cdot \sigma_s$$

The left hand side can also be expressed from the solid velocity  $\mathbf{v}$  using that  $\frac{\partial^2 \mathbf{U}}{\partial t^2} = \frac{\partial \mathbf{v}}{\partial t}$ . The advantage of using  $\mathbf{v}$  as the unknown will be discussed in chapter 4.

Therefore, the governing equation for the Linear Elasticity problem will be

$$\rho \frac{\partial \mathbf{v}}{\partial t} = \nabla \cdot \sigma_s$$

### 3.4 Linear Poroelasticity

In this section, the equations describing fluid flowing through an elastic, porous medium is presented. For a more detailed discussion, derivation and history within the field we refer to [11] on Linear Poroelasticity. To keep the mathematics as similar to the fluid case as possible, we use  $\mu$  and  $\lambda$  instead of the posision ratio. The equations describing linear poroelasticity are often described as Biot's equations.

#### 3.4.1 Fluid flow through a porous media

A porous medium is a material with pores in which fluid can flow. The principles of modeling porous flow consist of macroscopic averaging over the pores. The material part is often known as the skeleton, matrix or frame and in general all the pores will have different size and shape. In this section the skeleton is assumed rigid. The nature of the material defines whether we will be able to fully solve the problem with no-slip conditions on all skeleton parts, or if

some kind of volumetric averaging can be done. If the observer is interested in velocity variations on the scales of the pores, conventional fluid dynamics must be used. When there are many pores and channels, the complexity of the problem makes the full Navier-Stokes system difficult to solve. In these cases, macroscopic volume averaging is usually done, where the effects of the skeleton is modeled by introducing parameters constant over the material considered, such as permeability and conductivity.

These kinds of simplifications results in the famous Darcy's law, here generalized in three dimensions

$$\mathbf{v} = -\mu \mathbf{K} \cdot \nabla p \quad (3.7)$$

Where  $\mathbf{K}$  is the permability tensor, and  $\mu$  is the dynamics viscosity of the fluid. If the medium considered is isotropic, the permeability is a scalar value and (3.7) can be expressed as

$$\mathbf{v} = -\frac{K}{\mu} \nabla p$$

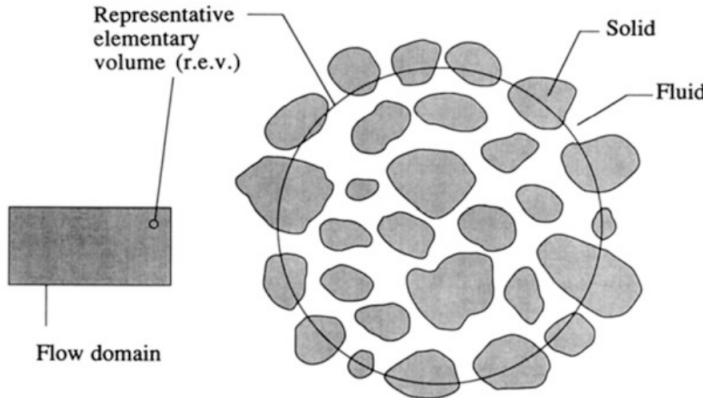


Figure 3.3: Representation of porous media where the averaging approach is used. From Nield and Bejan

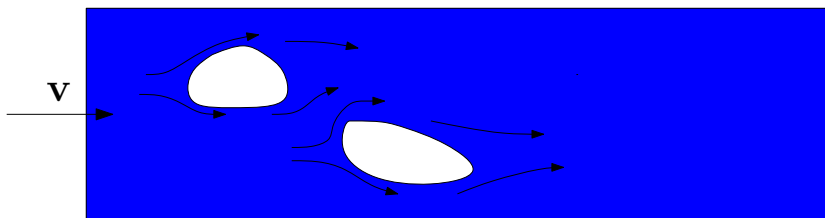


Figure 3.4: River flow around two islands representing the pores. The full Navier-Stokes system should be solved for this problem

### 3.4.2 Biot's equations

The stress tensor for the Biot problem is

$$\sigma_s = -pI + 2\mu\epsilon(\mathbf{U}) + \lambda\text{tr}(\epsilon(\mathbf{U}))I$$

Here  $\mu$  and  $\lambda$  are Lame's parameters for the solid. The parameter  $\alpha = \frac{K}{H}$  is known as the Biot-Willis coefficient.  $K$  is known as the drained bulk modulus, and  $\frac{1}{K}$  denotes compressibility.  $H$  is a poroelastic parameter describing how much the bulk volume changes due to a change in pore pressure while holding the applied stress constant. Again, conservation of momentum and mass, respectively, yields

$$-\mu\nabla^2\mathbf{U} - \lambda\nabla\nabla \cdot \mathbf{U} + \nabla p = \mathbf{F}_v \quad (3.8)$$

$$(\nabla \cdot \mathbf{U})_t - \nabla \cdot (\mu_f^{-1}\mathbf{K}\nabla p) = 0 \quad (3.9)$$

Where  $\mu_f$  is the dynamic viscosity of the fluid and the  $t$ -subscript denotes time derivative. As described in [12],  $-\mu^{-1}\mathbf{K}\nabla p$  represents the fluid velocity in the porous medium relative to the solid movement. In other words, the total fluid movement in the poroelastic medium is  $\mathbf{U}_t - \mu_f^{-1}\mathbf{K}\nabla p$ .  $\mathbf{K}$  is known as the permeability matrix. In an isotropic medium we can assume that  $\mathbf{K}$  is a scalar constant,  $K$ .

Equations (3.8)-(3.9) are nothing more than superpositioning of the two phases. The material derivatives in (3.8) has been dropped under the assumption that these terms are small. This assumption is known as a quasistatic approximation.

## 3.5 Descriptions of Motion

In the previous section, we saw that the stress tensor for elastic solids were linked to the total displacement from the stress-free configuration of the material. The stresses and velocity in the material will depend on the current deformation of the material with respect to the stress-free configuration. To this end, it will be convenient to provide the reader with two classical descriptions of a continuum in motion.

### 3.5.1 Lagrangian and Eulerian descriptions of motion

We consider a domain  $\Omega_{\mathbf{X}} \in \mathbb{R}^3$  consisting of material particles  $\mathbf{X}$ . The domain can undergo deformations, and the deformed domain,  $\Omega_{\mathbf{x}}$ , is the current configuration at time  $t$ .

We define the one-to-one mapping:

$$\begin{aligned} \beta : \Omega_{\mathbf{X}} \times [0, T] &\rightarrow \Omega_{\mathbf{x}} \times [0, T] \\ (\mathbf{X}, t) &\rightarrow \beta(\mathbf{X}, t) = (\mathbf{x}, t) \end{aligned}$$

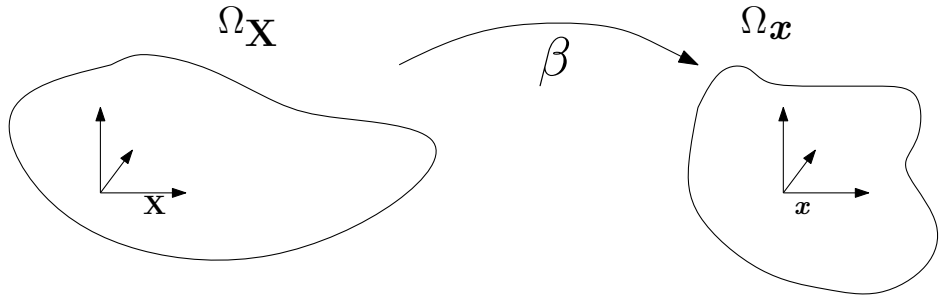


Figure 3.5: Lagrangian description of motion. The mapping  $\beta$  maps the reference coordinates to the spatial ones

Which takes any point  $\mathbf{X}$  in the reference configuration to a new position  $\mathbf{x} = \beta(\mathbf{X}, t)$  at time  $t$ . As the mapping is one-to-one, it is also possible to keep track of the history of the motion by the inverse,  $\beta^{-1}$ . The time is measured with the same variable,  $t$ , in both domains. The gradient of  $\beta$  with respect to  $(\mathbf{X}, t)$  can be written in matrix form as:

$$\frac{\partial \beta}{\partial (\mathbf{X}, t)} = \begin{pmatrix} \frac{\partial \mathbf{x}}{\partial \mathbf{X}} & \mathbf{v} \\ \mathbf{0}^T & 1 \end{pmatrix}$$

where the material velocity

$$\mathbf{v}(\mathbf{X}, t) = \frac{\partial \mathbf{x}}{\partial t} \Big|_{\mathbf{X}} \quad (3.10)$$

is the temporal change in the spatial variable  $\mathbf{x}$  while holding  $\mathbf{X}$  fixed.  $\mathbf{0}^T$  denotes a null vector.

The *Lagrangian* description, where we follow a fixed set of material particles as suggested by the mapping  $\beta$ , is often used. In the Lagrangian description all quantities are expressed in terms of the reference configuration  $\Omega_{\mathbf{X}}$  and time. In other words, even though the material is deformed, we can still compute displacements and particle velocities using the material coordinates  $\mathbf{X}$ . For instance, the displacement from the starting material configuration will be given as  $\beta(\mathbf{X}, t) - \mathbf{X}$  and the velocity as given in (3.10).

Because the grid coincides with the material coordinates, there are no convective terms in the Lagrangian description. In the context of Reynold's Transport theorem, the Lagrangian approach coincides with a moving control volume consisting of the same material points at all time. When a material undergoes large deformations or for instance vortices or turbulence occur, the material velocity from the Lagrangian point of view becomes difficult to handle.

In fluid mechanics the *Eulerian* description is the most used, which means that fluid flows through a fixed region in space and in each point we can measure various properties or quantities such as velocity, pressure and temperature. The conservation equations in the Eulerian description are expressed in terms of the spatial coordinates  $\mathbf{x}$  and time, and are neither connected to a reference configuration nor the material coordinates. Compared to the Lagrangian approach, large material deformations is not a problem, as material can enter and leave

the fixed domain. This movement of a material through a fixed region results in convective effects, and convection operators can often be problematic in computational fluid dynamics due to their non-symmetric nature.

### 3.5.2 The Arbitrary Eulerian Lagrangian description

To be able to couple the Lagrangian approach for the solid with the Eulerian approach for the fluid, we need some referential system, not attached to the material points neither totally fixed in space. This type of description is common in FSI analysis and is known as the *arbitrary Lagrangian-Eulerian* (ALE) description.

The following derivation is inspired by the the works on Arbitrary Lagrangian-Eulerian methods by Donea et. al in [13].

The need for an additional set of coordinates, an independent referential system with reference coordinates  $\chi$  is introduced. This introduces two new mappings to relate all the different configurations as shown in fig.

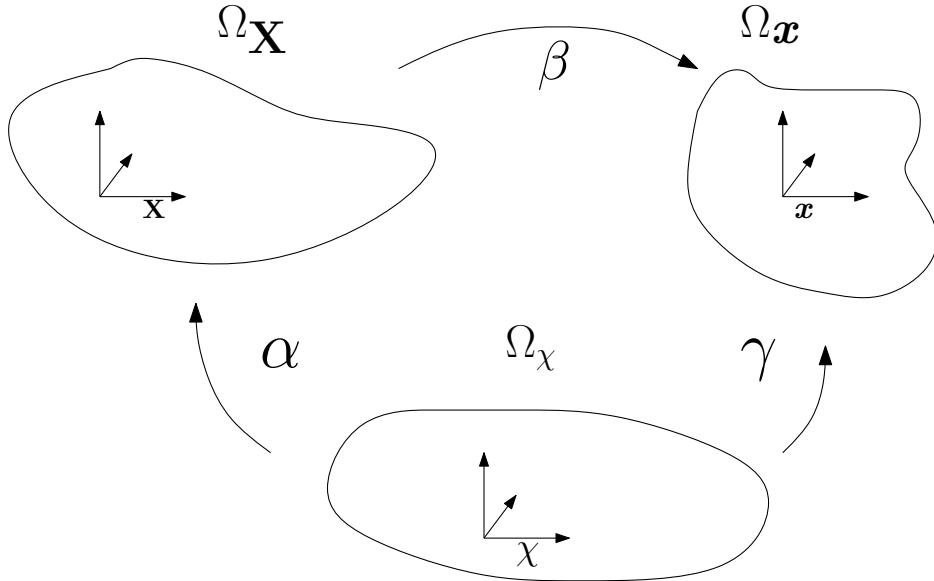


Figure 3.6: The three domains needed in the ALE formulation

The mappings are defined similarly to  $\beta$  as

$$\begin{aligned}\gamma &: \Omega_\chi \times [0, T] \rightarrow \Omega_x \times [0, T] \\ (\chi, t) &\rightarrow \gamma(\chi, t) = (x, t)\end{aligned}$$

and the gradient of  $\gamma$

$$\frac{\partial \gamma}{\partial(\chi, t)} = \begin{pmatrix} \frac{\partial \mathbf{x}}{\partial \chi} & \mathbf{w} \\ 0^T & 1 \end{pmatrix}$$

In addition,

$$\mathbf{w}(\chi, t) = \frac{\partial \mathbf{X}}{\partial t} \Big|_{\chi}$$

denotes the mesh velocity. Both the mesh and the material can move independently of the laboratory. More precise, relative to some referential point in space, the fluid moves with velocity  $\mathbf{v}$  and the domain moves with velocity  $\mathbf{w}$ .

To complete the relation between the different velocities, we define the inverse of  $\alpha$  directly:

$$\begin{aligned} \alpha^{-1} : \Omega_{\mathbf{X}} \times [0, T] &\rightarrow \Omega_{\chi} \times [0, T] \\ (\mathbf{X}, t) &\rightarrow \alpha^{-1}(\mathbf{X}, t) = (\chi, t) \end{aligned}$$

The gradient is given as

$$\frac{\partial \alpha^{-1}}{\partial(\mathbf{X}, t)} = \begin{pmatrix} \frac{\partial \chi}{\partial \mathbf{X}} & \hat{\mathbf{v}} \\ 0^T & 1 \end{pmatrix}$$

Where the velocity

$$\hat{\mathbf{v}}(\mathbf{X}, t) = \frac{\partial \chi}{\partial t} \Big|_{\mathbf{X}} \quad (3.11)$$

denotes the temporal change in the referential system while holding the material particle  $\mathbf{X}$  fixed. Therefore the velocity  $\hat{\mathbf{v}}$  can be interpreted as the particle velocity in the referential domain.

We use that  $\beta = \gamma \circ \alpha^{-1} = \gamma(\alpha^{-1}(\mathbf{X}, t))$  and obtain a relation between the different velocities by differentiating  $\beta$ .

$$\begin{aligned} \frac{\partial \beta}{\partial(\mathbf{X}, t)}(\mathbf{X}, t) &= \frac{\partial \gamma}{\partial(\chi, t)}(\alpha^{-1}(\mathbf{X}, t)) \frac{\partial \alpha^{-1}}{\partial(\mathbf{X}, t)}(\mathbf{X}, t) \\ &= \frac{\partial \gamma}{\partial(\chi, t)}(\chi, t) \frac{\partial \alpha^{-1}}{\partial(\mathbf{X}, t)}(\mathbf{X}, t) \end{aligned}$$

In matrix form this equation is written:

$$\begin{pmatrix} \frac{\partial \mathbf{x}}{\partial \mathbf{X}} & \mathbf{v} \\ 0^T & 1 \end{pmatrix} = \begin{pmatrix} \frac{\partial \mathbf{x}}{\partial \chi} & \mathbf{w} \\ 0^T & 1 \end{pmatrix} \begin{pmatrix} \frac{\partial \chi}{\partial \mathbf{X}} & \hat{\mathbf{v}} \\ 0^T & 1 \end{pmatrix}$$

After block-multiplication of the right hand side we end up with an equation relating all the different velocities:

$$\mathbf{v} = \frac{\partial \mathbf{x}}{\partial \chi} \cdot \hat{\mathbf{v}} + \mathbf{w}$$

To this end, it is convenient to define the convective velocity

$$\mathbf{c} := \mathbf{v} - \mathbf{w} = \frac{\partial \mathbf{x}}{\partial \chi} \cdot \hat{\mathbf{v}}$$

which is the relative velocity between the material and the mesh.

To obtain relation between quantities to formulate the balance equations, we let a scalar quantity,  $Q$  be defined as  $Q(\mathbf{x}, t)$ ,  $Q^*(\chi, t)$  and  $Q^{**}(\mathbf{X}, t)$  in the spatial, referential and material domains respectively.

To obtain a relation between the spatial description,  $Q$ , and material description  $Q^{**}$  we can utilize the previously described mapping  $\beta$ :

$$Q^{**}(\mathbf{X}, t) = Q(\beta(\mathbf{X}, t), t) = Q \circ \beta$$

The gradient of  $Q^{**}$  can then be computed as

$$\frac{\partial Q^{**}}{\partial(\mathbf{X}, t)}(\mathbf{X}, t) = \frac{\partial Q}{\partial(\mathbf{x}, t)}(\mathbf{x}, t) \frac{\partial \beta}{\partial(\mathbf{X}, t)}(\mathbf{X}, t) \quad (3.12)$$

$$\begin{pmatrix} \frac{\partial Q^{**}}{\partial \mathbf{X}} & \frac{\partial Q^{**}}{\partial t} \end{pmatrix} = \begin{pmatrix} \frac{\partial Q}{\partial \mathbf{x}} & \frac{\partial Q}{\partial t} \end{pmatrix} \begin{pmatrix} \frac{\partial \mathbf{x}}{\partial \mathbf{X}} & \mathbf{v} \\ 0^T & 1 \end{pmatrix} \quad (3.13)$$

After multiplication one can obtain the well known equation between material and spatial time derivatives:

$$\frac{\partial Q^{**}}{\partial t} = \frac{\partial Q}{\partial t} + \frac{\partial Q}{\partial \mathbf{x}} \cdot \mathbf{v} \quad (3.14)$$

To ease notation we now recognize the material and spatial time derivatives  $\frac{\partial Q^{**}}{\partial t} = \frac{\partial Q}{\partial t} \Big|_{\mathbf{X}}$ ,  $\frac{\partial Q}{\partial t} = \frac{\partial Q}{\partial t} \Big|_{\mathbf{x}}$ , and define the material and spatial derivatives the following way

$$\frac{d}{dt} := \frac{\partial}{\partial t} \Big|_{\mathbf{x}} \quad \frac{\partial}{\partial t} := \frac{\partial}{\partial t} \Big|_{\mathbf{x}}$$

The relation (3.14) can now be written in a form probably already known to the reader

$$\frac{dQ}{dt} = \frac{\partial Q}{\partial t} + \mathbf{v} \cdot \nabla Q \quad (3.15)$$

The next step is to relate the material and the referential description of the quantity,  $Q^{**}$  and  $Q^*$  respectively, by the mapping  $\alpha$ . This relation is written as

$$Q^{**} = Q^* \circ \alpha^{-1}$$

By proceeding the exact same way as in (3.12) and (3.13) the relation between material and referential time derivatives is written

$$\frac{\partial Q^{**}}{\partial t} = \frac{\partial Q^*}{\partial t} + \frac{\partial Q^*}{\partial \chi} \cdot \hat{\mathbf{v}}$$

If we rather want to express the spatial derivative of  $Q^*$  in the spatial domain, we can use the definition of  $\hat{\mathbf{v}}$  from (3.11) to end up with

$$\frac{\partial Q^{**}}{\partial t} = \frac{\partial Q^*}{\partial t} + \frac{\partial Q}{\partial \mathbf{x}} \cdot \mathbf{c}$$

This equation can be written in more common notation, and the following is known as *The fundamental ALE equation*

$$\frac{dQ}{dt} = \frac{\partial Q}{\partial t} \Big|_{\chi} + \mathbf{c} \cdot \nabla Q \quad (3.16)$$

and states that the time derivative in the material configuration equals its local (referential) derivative plus a convective term taking into account the relative difference in velocity between the two systems. It should be noted that the relations presented also holds for vector quantities.

Also, by combining equations (3.15) and (3.16), we can relate the spatial time derivative with the referential time derivative as

$$\frac{\partial Q}{\partial t} = \frac{\partial Q}{\partial t} \Big|_{\chi} - \mathbf{w} \cdot \nabla Q \quad (3.17)$$

## 3.6 Balance equations in the ALE framework

To obtain appropriate balance equations in the ALE framework we start by noting that the balance equations can be written in terms of the material derivatives as

$$\frac{d\rho}{dt} = \frac{\partial \rho}{\partial t} + \mathbf{v} \cdot \nabla \rho = -\rho \cdot \nabla \mathbf{v}$$

$$\rho \frac{d\mathbf{v}}{dt} = \rho \left( \frac{\partial \mathbf{v}}{\partial t} + (\mathbf{v} \cdot \nabla) \mathbf{v} \right) = \nabla \cdot \boldsymbol{\sigma}$$

By using (3.17), the spatial time derivatives can be replaced to obtain equations for the ALE framework:

$$\frac{\partial \rho}{\partial t} \Big|_{\chi} + \mathbf{c} \cdot \nabla \rho = -\rho \cdot \nabla \mathbf{v}$$

$$\rho \left( \frac{\partial \mathbf{v}}{\partial t} \Big|_{\chi} + (\mathbf{c} \cdot \nabla) \mathbf{v} \right) = \nabla \cdot \boldsymbol{\sigma}$$

Which shows that all one have to do in order to transform the Eulerian form of the balance equations into the ALE formulation is to replace the convective velocity with the relative velocity between the material and the mesh.

### 3.6.1 Mesh updating

The velocity  $\mathbf{w}$  can be seen as the mesh velocity when a computational mesh is used. In FSI, the ALE framework provides flexibility to combine the Lagrangian and Eulerian descriptions of motion. On the structural part, as well

as on the fluid-structure interface, the domain  $\Omega_s$  consists of the same material particles at all times and moves exactly with the material points within the structure. That is,  $\mathbf{v}_s = \mathbf{w}_s$ . The fluid domain has to follow the changes on the fluid-structure interface. Other than that the mesh velocity in the fluid domain is arbitrary in principle, but the choice of mesh velocity in the fluid domain is important for the accuracy of the solver. In general, important aspects to consider is distortion and squeeze of each element in the fluid domain.

A Laplacian smoothing algorithm is used to update the mesh, consisting of solving a Laplace (or Poisson) equation for the mesh displacement in the fluid. The method is a mesh regularization method where the lines in the mesh have equal potential. This method was first introduced by Winslow in 1963 [14].

### 3.7 Fluid Structure Interaction

In the case of an Newtonian incompressible fluid the mathematical problem consists of solving

$$\left. \begin{array}{l} \rho \left( \frac{\partial \mathbf{v}}{\partial t} + ((\mathbf{v} - \mathbf{w}) \cdot \nabla) \mathbf{v} \right) = \nabla \cdot \sigma_f(\mathbf{v}, p) \\ \nabla \cdot \mathbf{v} = 0 \\ \nabla^2 \mathbf{U} = 0 \end{array} \right\} \text{in } \Omega_f^t$$

$$\left. \begin{array}{l} \rho \frac{\partial \mathbf{v}}{\partial t} = -\nabla \cdot \sigma_s(\mathbf{U}) \\ \mathbf{w} = \mathbf{v} \end{array} \right\} \text{in } \Omega_s^t$$

In the case of fluid interacting with a solid structure, no material can cross the moving boundary and thus the fluid and solid velocity must be equal on the interface between the fluid and the solid. In general, one have to ensure mass conservation on the boundary. In addition the forces acting on the surface must be equal. A difference in forces from each material on the interface would result in infinite acceleration on the infinitely thin surface. Mathematically, these two conditions can be stated as

$$\left. \begin{array}{l} \sigma_f \cdot \mathbf{n} = \sigma_s \cdot \mathbf{n} \\ \mathbf{v}_f = \mathbf{v}_s \end{array} \right\} \text{on } \Gamma^t$$

And will be used at all interfaces in FSI simulations. Kinematic or dynamic boundary conditions will be needed on the other boundaries as well, but will differ depending on the problem considered.



# Chapter 4

# Numerical Methods

## 4.1 The Finite Element Method

The theory presented in this section is partly inspired by the works of Langtangen in "Finite Element Method - INF5620 lecture notes" [15]

Consider the Poisson-equation

$$-\nabla^2 v = f \quad \text{in } \Omega \quad (4.1)$$

$$v = v_0 \quad \text{on } \partial\Omega_D \quad (4.2)$$

$$\frac{\partial v}{\partial n} = g \quad \text{on } \partial\Omega_N \quad (4.3)$$

where  $\Omega \in \mathbb{R}^d$  is a domain,  $v = v(x)$  is an unknown function and  $f$  is a source function. The boundary,  $\partial\Omega$  is divided into two parts.  $\partial\Omega_D$  for the Dirichlet boundary condition, and  $\partial\Omega_N$  for the Neumann condition.

### 4.1.1 Variational formulation

(4.1) is known as the strong form of the equation. To reformulate the problem and state a weak formulation we multiply the equation with a test function,  $\phi \in \hat{V}$ , where  $\hat{V}$  is some function space, and integrate over the domain. Weak formulations are important in the sense that differential equations can be transformed into systems of linear equations. In the rest of this text the following notation is used for the inner product of two functions

$$(v, \phi)_\Omega = \int_\Omega v \phi \, dx$$

By multiplying (4.1) with a test function,  $\phi$  and integrating over the domain, the weak form is obtained

$$(\nabla^2 v + f, \phi)_\Omega = 0 \quad \forall \phi \in \hat{V}$$

We are now searching for a  $v$  to satisfy the weak form instead of the strong. This equation should hold for all  $\phi$  in the function space  $\hat{V}$ . The trial function does not necessarily have to lie in the same function space, in general  $v \in V$ .

In this thesis we will use two Sobolov spaces (named after the Russian mathematician Sergei Sobolov) widely used in Finite Element computing. For these definitions to be valid, we assume that the functions  $v$  are all **—locally integrable** and in the case of definition (4.2), has one **weak derivative**. For more details on weak derivatives and the generalized concept of Sobolev spaces and functional analysis, we refer to the textbook by Brenner and Scott [16].

**Definition 4.1** *Let  $\Omega$  be an open subset of  $\mathbb{R}$  with a piecewise smooth boundary. We then define the  $L^2$ -norm as follows*

$$\|v\|_{L^2(\Omega)} = (\int_{\Omega} v^2 dx)^{\frac{1}{2}}$$

*The corresponding  $L^2$ -space is defined via*

$$L^2(\Omega) = \{v : \Omega \rightarrow \mathbb{R} \mid \int_{\Omega} v^2 dx < \infty\}$$

**Definition 4.2** *Let  $\Omega$  be an open subset of  $\mathbb{R}$  with a piecewise smooth boundary. We then define the  $H^1$ -norm as follows*

$$\|v\|_{H^1(\Omega)} = (\int_{\Omega} [v^2 + (\nabla v)^2] dx)^{\frac{1}{2}}$$

*The corresponding  $H^1$ -space is defined via*

$$H^1(\Omega) = \{v : \Omega \rightarrow \mathbb{R} \mid \int_{\Omega} [v^2 + (\nabla v)^2] dx < \infty\}$$

In other words, using functions from these spaces, we can have some assurance that the integrals involved in the variational form are bounded. By the divergence theorem, a generalized concept of integration by parts we can state the variational problem as follows: find  $v \in V$  such that

$$(\nabla v, \nabla \phi)_{\Omega} = (f, \phi)_{\Omega} + (g, \phi)_{\partial\Omega_N} \quad \forall \phi \in \hat{V} \quad (4.4)$$

Where we have used that  $\frac{\partial v}{\partial n} = g$  on  $\partial\Omega_N$ . (4.4) is known as the variational formulation of the Poisson problem. The left hand side is known as the bilinear form while the right hand side is the linear form. In generic form the equation can be written

$$a(v, \phi) = L(\phi) \quad (4.5)$$

The first derivative of  $v$  appears in the variational form. A common choice is then

$$\begin{aligned} V &:= \{v \in H^1(\Omega) : v = v_0 \text{ on } \partial\Omega_D\} \\ \hat{V} &:= \{v \in H^1(\Omega) : v = 0 \text{ on } \partial\Omega_D\} \end{aligned}$$

In other words, the trial and test functions are in the same function space, except on the boundary.

### 4.1.2 Finite elements

The next step is to approximate  $v$  with a sum of basisfunctions in the finite-dimensional function space,  $V = \text{span}\{\phi_0, \phi_1, \dots, \phi_N\}$ . Here,  $\phi_i$  represents the basis functions and we search for a solution  $v_h \in V$  such that  $v_h$  can be written as a linear combination of the basis functions. The first step in the finite element method consists of dividing the domain into smaller parts

$$\Omega = \Omega_0 \cup \Omega_1 \cup \dots \cup \Omega_{N_e}$$

where  $N_e$  is the number of elements. Each element have a number of nodes within them depending on what type of basis functions to be used. Let's first consider the continuous Galerkin basis functions, in a one-dimensional domain. There is exactly one basisfunction for each node located at  $x_i$ . These basis functions have the property that

$$\phi_i(x_j) = \begin{cases} 1 & \text{for } i = j \\ 0 & \text{for } i \neq j \end{cases}$$

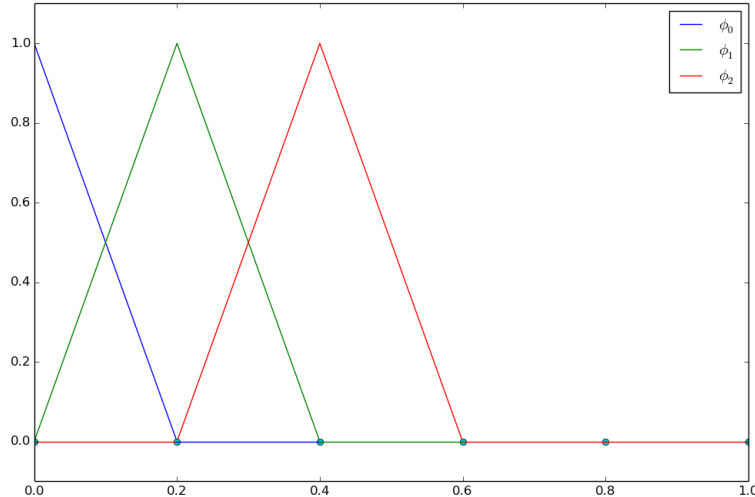


Figure 4.1: The three first linear basis functions on the unit interval divided uniformly into 5 elements,  $\Omega_0 = [0, 0.2]$ ,  $\Omega_1 = [0.2, 0.4]$  and so on. In the case of Dirichlet Boundary conditions at  $x = 0$ ,  $\phi_0$  will not be included in the function space

That is, the basis functions  $\phi_i$  are zero on all nodes except at node  $i$ . Each basis function is constructed by taking the Lagrange-polynomial which is 1 at the given node and 0 on the neighboring nodes. Note that the basis functions are two Lagrange-polynomials "pieced together" at the node where it's value is 1. For the rest of the domain the basis functions are defined to be 0.

Now, let's return to the original problem (4.1)-(4.3) in scalar form. We start by approximating  $v$  as a linear combination of all the basis functions.

$$v_h = \sum_{i=0}^N c_i \phi_i$$

The definitions of  $v_h$  and  $V$  now give rise to a linear system. Using the Einstein summation convention,  $x_i y_i = \sum_0^N x_i y_i$ , the discretized version of (4.4) is now written

$$-c_i (\nabla \phi_i, \nabla \phi_j)_\Omega = (f, \phi_j)_\Omega - (g, \phi_j)_{\partial \Omega_N}$$

In the case of Dirichlet boundary conditions all test functions  $\phi_j$  will take the value 0 on  $\partial \Omega_D$  and the linear system will be adjusted to take these boundary conditions into account.

The system can be written in matrix form, and in the end the problem consists of solving the linear system

$$A_{i,j} c_i = b_j$$

### 4.1.3 Implementation in FEniCS

When the variational form has been carried out, implementation in FEniCS is relatively simple. The programs in this study are written in the Python programming language. When programming with Python, we first need to import dolfin to access the DOLFIN library, containing classes convenient and efficient for finite element computing. In Python the full library can be imported as simple as

```
from dolfin import *
```

Now, let's focus our attention on solving the following problem:

$$\begin{aligned} \nabla^2 v &= 20x & \text{in } \Omega \\ v(0, y) &= 0, \quad v(1, y) = 1 \\ \frac{\partial v(x, 0)}{\partial n} &= \frac{\partial v(x, 1)}{\partial n} = 0 \end{aligned}$$

Where  $\Omega$  is the unit square,  $\Omega = [0, 1] \times [0, 1]$

First of all we need to define the computational mesh.

```
mesh = UnitSquareMesh(10, 10)
```

The class `UnitSquareMesh` initializes a mesh with triangular cells. The mesh consists of  $n \times m$  squares depending on the arguments,  $n$  and  $m$ , sent into the constructor. Each of these squares are divided on the diagonal to form two triangles, and these triangles are the computational cells. In this case we get the unit square divided into  $10 \times 10$  smaller squares and thus the total number of triangles, or cells, will be 200.

The next thing to do is to define an appropriate function space for the test functions. The solution will be a linear combination of these functions and will be in (almost) the same function space.

```
V = FunctionSpace(mesh, 'CG', 1)
```

The function space needs a domain, type of element, and the degree of the element. In this case we use Continuous Galerkin elements ('CG') with degree 1. These basis functions are visualized in Figure 4.1

We can then define our test- and trial functions  $v$  and  $\phi$

```
v = TrialFunction(V)
phi = TestFunction(V)
```

Note that the test- and trial function seem to be in the exact same function space. This is the case except when imposing Dirichlet boundary conditions. The functions  $f$ ,  $v_0$  and  $g$  can be defined by using the 'Constant' or 'Expression' classes. We set  $f = 20x$  and use Dirichlet boundary conditions,  $v(0, y) = 0$ ,  $v(1, y) = 1$  and Neumann conditions  $\frac{\partial v(x, 0)}{\partial n} = \frac{\partial v(x, 1)}{\partial n} = 0$ . The homogenous Neumann condition is simple in the finite element method as the terms appearing after integration by parts can be dropped. If this is not the case, we can insert  $g$  for  $\frac{\partial u}{\partial n}$  on the boundary integral appearing in the variational form. When the Neumann conditions are incorporated this way we say that the boundary conditions are weakly imposed. Functions (or classes) describing the boundaries must also be defined:

```
f = Expression('20*x[0]')
def boundary0(x, on_bnd):
    return on_bnd and near(x[0], 0.0)
def boundary1(x, on_bnd):
    return on_bnd and near(x[0], 1.0)

bc0 = DirichletBC(V, 0.0, boundary0)
bc1 = DirichletBC(V, 1.0, boundary1)
bcs = [bc0, bc1]
```

Note that ' $x[0]$ ' means first dimension in space, ' $x[1]$ ' means second dimension and so on. The Dirichlet conditions are put in a list. Next, the variational form is defined, and when solving for a function  $v$ , the boundary conditions are added to the "magic" `solve` function.

```
F = inner(grad(v), grad(phi))*dx - inner(f, phi)*dx
v = Function(V)
solve(lhs(F)==rhs(F), v, bcs)
plot(v)
```

The functions `lhs` and `rhs` separates the form `F` into the left hand side, equivalent to the bilinear form and to the right hand side, equivalent to the linear form. Specifying the full form `F` is simple and convenient when the equations are short and simple. If we want to relate the code to the mathematics as written in (4.5) we can, define these forms manually.

```
a = inner(grad(v),grad(phi))*dx
L = inner(f,phi)*dx
v = Function(V)
solve(a==L,v,bcs)
```

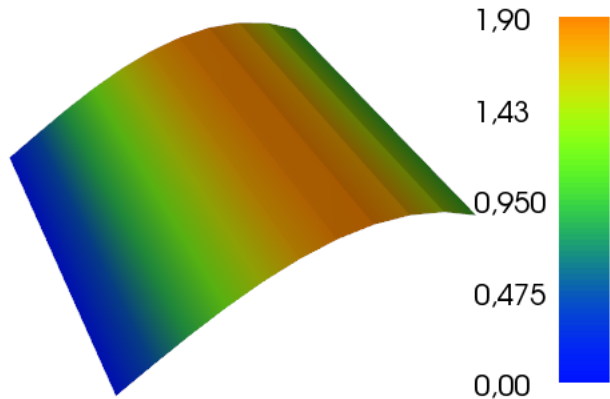


Figure 4.2: Plot of the computed solution

The plot in the figure is slightly rotated. The solution is independent of  $y$ -position, as expected.

## 4.2 A benchmark FSI-problem

Within CFD, a benchmark is a configuration or a test case which should help test and compare different numerical methods and code implementations. A classical Fluid Dynamics problem regarding flow around a circular cylinder has been under vast research the last 50 years, working as a test case for both laminar and turbulent flows. One of the most cited benchmark proposals for this case is the problem described by Michael Schafer et. al in 1996 [17]. The research group still focus on these kinds of problems and one of the co-authors of the 1996 paper, Stefan Turek, together with Jaroslav Hron has proposed a similar benchmark for FSI solvers, consisting of the exact same domain and rigid cylinder, but now with an elastic flag attached to it [18].

The first results presented will contain a validation of the present FSI-solver implemented in FEniCS compared to the results of Turek and Hron in their benchmark proposal.

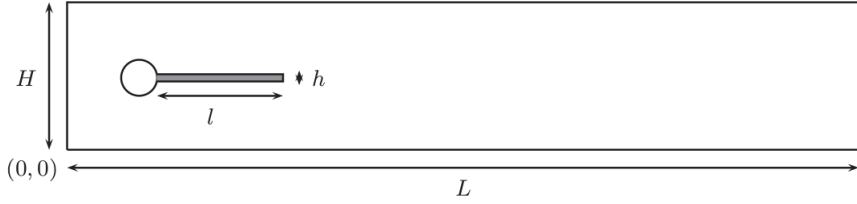


Fig. 1. Computational domain

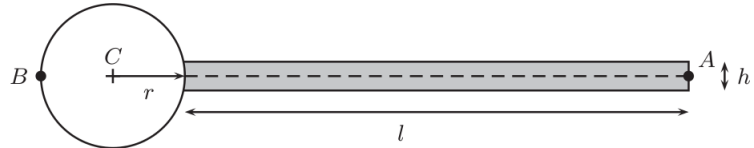


Fig. 2. Detail of the structure part

Figure 4.3: The Domain as published in [18]

A proper validation of a FSI solver requires separate verification of the fluid and structural parts as well as coupled tests. In the present study we solve the system of equations with a *monolithic* approach, i.e. full coupling between the fluid and solid. The alternative would be a *partitioned* approach, where the fluid and solid equations are solved separately. For instance, one can solve the fluid equations independently and then proceed by solving the solid equation with prescribed stress on the interface computed from the fluid solution. Iteration back and forth would be needed until convergence.

The fully coupled monolithic scheme is usually preferred with respect to accuracy and stability. Also, when the systems are strongly coupled in nature, i.e. the solid movement is affected by the fluid movement and vice versa, a monolithic scheme would be advantageous. The partitioned approach, on the other hand, can benefit from numerous previous studies where efficiency and stability for various solution techniques have been investigated. See e.g. [19] for a short review. In addition, solving many smaller matrix systems will be way faster than solving one large system with the same number of unknowns.

#### 4.2.1 Domain, Initial- and boundary conditions

The origin is set at the bottom left corner. We also set:

- The channel height,  $H = 0.41$
- The channel length,  $L = 2.5$
- The circle center  $C = (0.2, 0.2)$
- The right bottom corner of the elastic structure has position  $(0.6, 0.19)$
- The elastic structure has length,  $l=0.35$  and height  $h=0.02$

- At the left boundary, the inlet, of the channel, we set a prescribed parabolic

velocity profile

$$\mathbf{v}_{\text{in}}(0, y) = 1.5\bar{v}_0 \frac{y(H-y)}{(\frac{H}{2})^2}$$

- In the case of unsteady flow a smooth increase in time is used:

$$\mathbf{v}_{\text{in}}(t, 0, y) = \begin{cases} \mathbf{v}_{\text{in}}(0, y) \frac{1-\cos(\frac{\pi}{2}t)}{2} & \text{if } t < 2.0 \\ \mathbf{v}_{\text{in}}(0, y) & \text{otherwise} \end{cases}$$

- On the outlet, the condition  $\sigma \cdot \mathbf{n} = 0$  is applied - On rigid walls the no-slip condition is used - On the interface,  $\Gamma^t$ , the previously described coupling conditions are applied:

$$\left. \begin{array}{l} \sigma_f \cdot \mathbf{n} = \sigma_s \cdot \mathbf{n} \\ \mathbf{v}_f = \mathbf{v}_s \end{array} \right\} \text{on } \Gamma^t$$

In addition to the interface,  $\Gamma^t$ , it may be convenient to define the fluid boundary,  $\partial\Omega_f^t$  consisting of the outer rectangle and the part of the circle in contact with the fluid, and the solid boundary,  $\partial\Omega_s^t$  consisting of the circle in contact with the solid.

#### 4.2.2 CFD tests

For the CFD tests we perform tests treating the flag as a rigid object. This can be done by changing the structural parameters, or simply by adjust the mesh to include the fluid domain only. In this validation we choose the latter. We show convergence with Mesh, where mesh 0 is the coarsest version. The **Ref.** are the reference values as given in the original benchmark paper.

Parameter	CFD1	CFD2	CFD3
$\rho_f [10^3 \frac{\text{kg}}{\text{m}^3}]$	1	1	1
$\nu_f [10^{-3} \frac{\text{m}^2}{\text{s}}]$	1	1	1
$\bar{v}_0$	0.2	1	2
$\text{Re} = \frac{Ud}{\nu_f}$	20	100	200

Table 4.1: Parameters for the CFD test cases

cells	dofs	Drag	Lift
1334	6443	13.9344	1.0980
5336	24892	14.1165	1.0836
21344	97808	14.1865	1.0944
<b>Ref.</b>		<b>14.29</b>	<b>1.119</b>

Table 4.2: Results for CFD1

cells	dofs	Drag	Lift
1334	6443	130.092948352	10.9117261826
5336	24892	134.43022177	10.473965217
21344	97808	135.777285175	10.7118857057
<b>Ref.</b>		<b>136.7</b>	<b>10.53</b>

Table 4.3: Results for CFD2

cells	dofs	Drag	Lift
1334	6443	$391.305 \pm 2.039$	$-28.536 \pm 200.149$
5336	24892	$428.769 \pm 5.735$	$-18.001 \pm 429.410$
21344	97808	1	2
<b>Ref.</b>		<b><math>439.45 \pm 5.6183</math></b>	<b><math>-11.893 \pm 437.81</math></b>

Table 4.4: Results for CFD3 for  $\Delta t = 0.0005$  and  $\Delta t = 0.0001$ 

#### 4.2.3 CSM tests

The structural tests are performed by adding the gravitational force to the structural part only. The CSM3 test is computed as a time-dependent case, starting from the initial position while CSM1 and CSM2 are Steady State (SS) solutions. For CSM3, the total energy is not conserved as the Backward Euler scheme used to discretize in time slightly reduces the amplitude for oscillating solutions. For this reason, a third parameter of interest is included in the results, namely the reduction of amplitude from one cycle to the next. From the reference results it appears that the flag bounces above the initial position in steady state, meaning that some energy must have been added due to their choice of scheme. This is also clear when closely examining the attached plots. This was not further discussed, and no time-dependent amplitude was reported. The temporal discretization in the original benchmark proposal was done by the Crank-Nicholson scheme, which in general have better conservation properties than the Backward-Euler scheme but is known to be less stable [20]

Parameter	CSM1	CSM2	CSM3
$\rho_s [10^3 \frac{\text{kg}}{\text{m}^3}]$	1	1	1
$\nu_s$	0.4	0.4	0.4
$\mu_s [10^6 \frac{\text{m}^2}{\text{s}}]$	0.5	2	0.5
$g [\frac{\text{m}^2}{\text{s}}]$	2	2	2

Table 4.5: Parameters for the CSM test cases

cells	dofs	$U_x$ of A [ $10^{-3}$ ]	$U_y$ of A [ $10^{-3}$ ]
738	4596	-12.410569	-60.599246
2952	17305	-12.419505	-60.622920
11808	67077	-12.422290	-60.630433
<b>Ref.</b>		<b>-7.187</b>	<b>-66.10</b>

Table 4.6: Results for CSM1

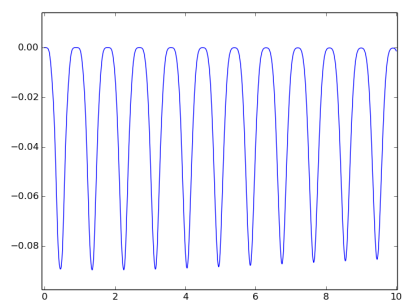
cells	dofs	$U_x$ of A [ $10^{-3}$ ]	$U_y$ of A [ $10^{-3}$ ]
738	4596	-0.92479395	-16.853778
2952	17305	-0.92558954	-16.861757
11808	67077	-0.92583356	-16.864252
<b>Ref.</b>		<b>-0.4690</b>	<b>-16.97</b>

Table 4.7: Results for CSM2

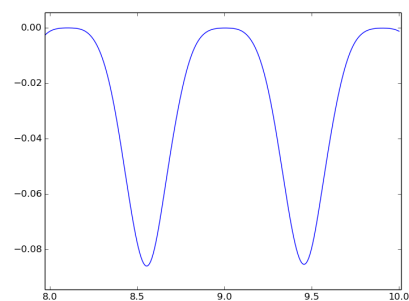
cells	dofs	$U_x$ of A [ $10^{-3}$ ]	$U_y$ of A [ $10^{-3}$ ]	Amp reduction y (%)
738	4596	-44.175 $\pm$ 44.007	-72.712 $\pm$ 65.281	5.4
2952	17305	-44.176 $\pm$ 44.001	-72.720 $\pm$ 65.281	5.4
11808	67077	-44.177 $\pm$ 44.001	-72.720 $\pm$ 65.281	5.4
<b>Ref.</b>		<b>-14.305 <math>\pm</math> 14.305</b>	<b>-63.607 <math>\pm</math> 65.160</b>	

cells	dofs	$U_x$ of A [ $10^{-3}$ ]	$U_y$ of A [ $10^{-3}$ ]	Amp reduction y (%)
738	4596	-44.631 $\pm$ 44.628	-69.702 $\pm$ 69.290	0.3
2952	17305	-44.633 $\pm$ 44.629	-69.701 $\pm$ 69.289	0.3
11808	67077	-44.094 $\pm$ 44.091	-69.703 $\pm$ 69.289	0.3
<b>Ref.</b>		<b>-14.305 <math>\pm</math> 14.305</b>	<b>-63.607 <math>\pm</math> 65.160</b>	

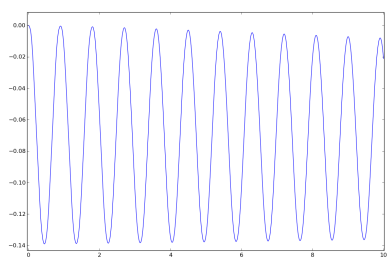
Table 4.8: Results for CSM3,  $\Delta t = 0.01, 0.001$



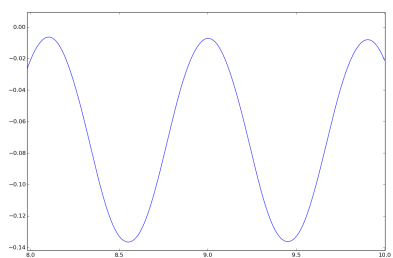
(a) displacement x vs time



(b) displacement x vs time



(c) displacement y vs time



(d) displacement y vs time

#### 4.2.4 FSI tests

Parameter	FSI1	FSI2	FSI3
$\rho_f [10^3 \frac{\text{kg}}{\text{m}^3}]$	1	1	1
$\nu_f [10^{-3} \frac{\text{m}^2}{\text{s}}]$	1	1	1
$\bar{v}_0$	0.2	1	2
$\text{Re} = \frac{Ud}{\nu_f}$	20	100	200

Parameter	FSI1	FSI2	FSI3
$\rho_s [10^3 \frac{\text{kg}}{\text{m}^3}]$	1	10	1
$\nu_s$	0.4	0.4	0.4
$\mu_s [10^6 \frac{\text{m}^2}{\text{s}}]$	0.5	0.5	2

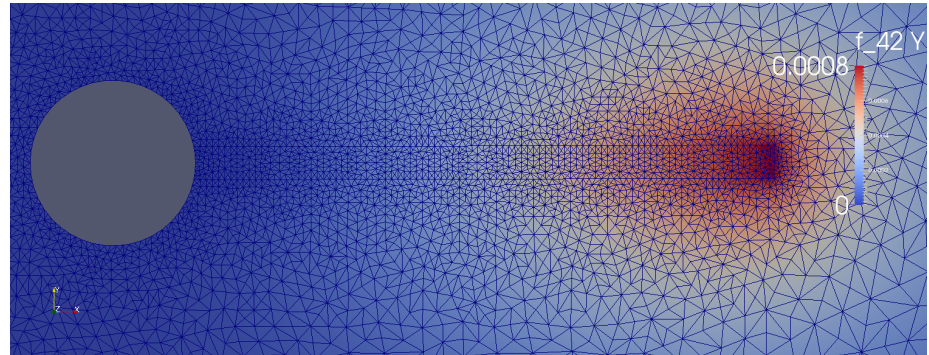


Figure 4.5: Steady State displacement in y-direction for the FSI1 test case for the medium refinement version of the mesh. Note that the mesh around the structural part also has been slightly adjusted

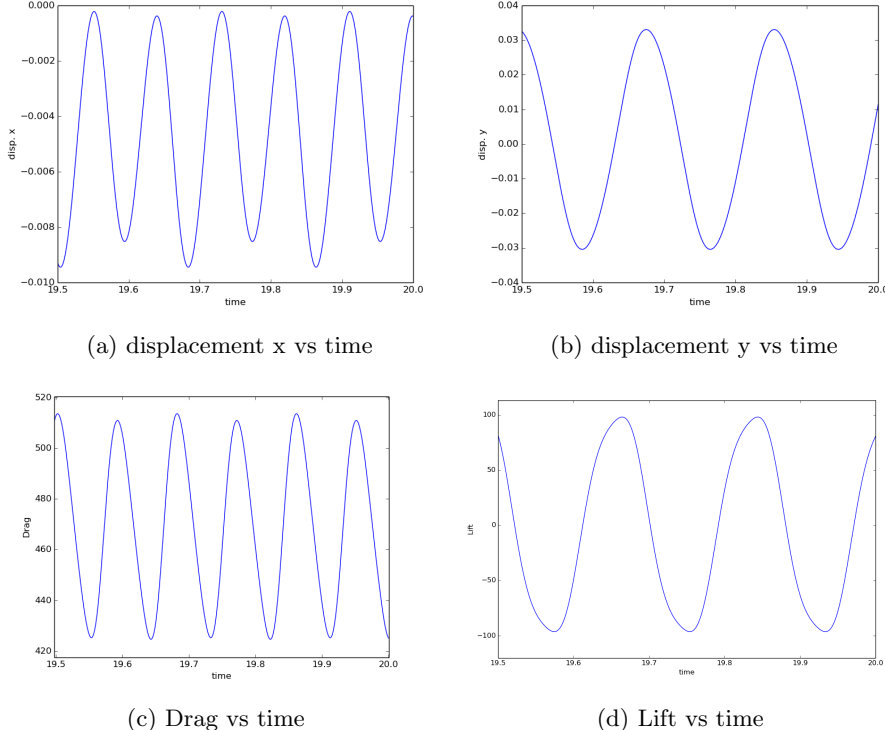
cells	dofs	$U_x$ of A $[10^{-3}]$	$U_y$ of A $[10^{-3}]$	Drag	Lift
2698	15329	0.015596	0.74221	14.0876279441	0.756130219216
10792	60336	0.017738	0.77686	14.1777783843	0.763145083966
43168	239384	0.019824	0.79558	14.1869409712	0.758109277348
<b>Ref.</b>		<b>0.0227</b>	<b>0.8209</b>	<b>14.295</b>	<b>0.7638</b>

Table 4.9: Results for FSI1

- note: Hron, Turek,  $\Delta t = 0.0005$ , we used  $\Delta t = 0.0003$ .

cells	dofs	$U_x$ of A [ $10^{-3}$ ]	$U_y$ of A [ $10^{-3}$ ]	Drag	Lift
2698	15329	$-4.33 \pm 4.54$	$1.40 \pm 29.96$	$441.45 \pm 33.15$	$-2.30 \pm 178.00$
10792	60336	$-4.84 \pm 4.62$	$1.27 \pm 31.74$	$469.11 \pm 44.50$	$0.92 \pm 97.27$
43168	239384				
<b>Ref.</b>		<b><math>-2.69 \pm 2.53</math></b>	<b><math>1.48 \pm 34.38</math></b>	<b><math>457.3 \pm 22.66</math></b>	<b><math>2.22 \pm 149.78</math></b>

Table 4.10: Results for FSI3



Numbers for FSI3: Ux: Max = 0.0002099, Min = -0.008879  
 Uy: Max = 0.03136, Min = -0.02856  
 Drag: Max = 474.6, Min = 408.3  
 Lift: Max = 175.7, Min = -180.3 (174.4, -177.0)

Frequency, 0.1795 /s for medium mesh.

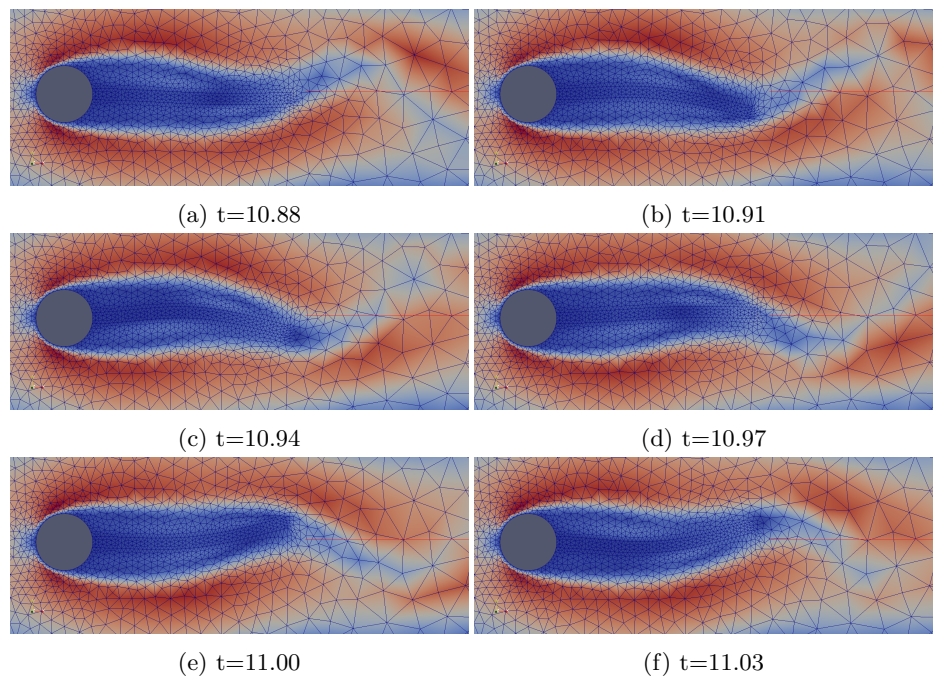


Figure 4.7: The colormap shows the magnitude of the velocity around the flag at six different states of time in fully developed flow on the coarsest mesh. Maximum velocity reaches 4.37. The mesh consists of a smooth curve at the interface, and the domains are separated beforehand in FEniCS

## 4.3 Fluid Structure Interaction using the Finite Element method

The solver was implemented from scratch in Python using the DOLFIN library. FSI solvers within the FEniCS framework exists, e.g. under Unicorn or CBC.twist. For instance, Selin [21] implemented a partitioned solver in FEniCS in his PhD-thesis, using the already existing modules for solving fluid flow and structural deformations separately (CBC.Flow and CBC.Twist). With the implementation presented here, it will be easier to adjust the solver with respect to the model. The equations can be changed whether we want the spinal cord to be porous, elastic, poroelastic or viscoelastic. The use of two separate solvers is also problematic for the monolithic approach, when all equations should be solved simultaneously. On the other hand, solvers implemented by experienced and skilled research groups will probably be a lot more efficient and should already have been validated.

In the rest of this section, we give a brief explanation to the mathematics and implementation in FEniCS. In the previous example we saw the close link between code and mathematics. :

$$\begin{aligned} a(\mathbf{v}, \Phi) &= (\nabla \mathbf{v}, \nabla \Phi)_{\Omega} \\ L(\mathbf{v}) &= (\mathbf{f}, \Phi)_{\Omega} \end{aligned}$$

Translates to

```
a = inner(grad(v), grad(phi))*dx
L = inner(f, phi)*dx
```

In deriving variational forms, we try to keep this close link by recalling the symbols used for velocity ( $\mathbf{v}$ ), total displacement ( $\mathbf{U}$ ), pressure ( $p$ ), and mesh velocity, ( $\mathbf{w}$ ). Also recall that in the solid the mesh moves exactly with the velocity of the structure so  $\mathbf{w}_s = \mathbf{v}_s$

### 4.3.1 Temporal discretization

In order not to overload this thesis with notation and superscripts, we have used the notation  $\mathbf{v} := \mathbf{v}^{n+1}$  to denote the value of a function at the next time-step. Similarly, we define  $\mathbf{v}^{(1)} := \mathbf{v}^n$  to denote the (known) value of a function at the present time step.

The total displacement  $\mathbf{U}$  can be expressed as a function of the displacement from the previous time step,  $\mathbf{U}^{(1)}$ , and the mesh velocity  $\mathbf{w}$ . We have used an implicit scheme in time, i.e,  $(\frac{\partial \mathbf{v}}{\partial t})^{n+1} \approx \frac{\mathbf{v}^{n+1} - \mathbf{v}^n}{\Delta t}$ , and  $\mathbf{U} = \mathbf{U}^{(1)} + \Delta t \mathbf{w}$ .

### 4.3.2 Spatial discretization

When dealing with nonlinear equations, such as the Navier-Stokes equation, *linearization* is needed in order to solve the equations. In the nonlinear terms, we simply replace one (or more) of the unknown  $\mathbf{v}$ 's with a "guess" to get an

equation linear in  $\mathbf{v}$ . This guess is denoted as  $\mathbf{v}^{(0)}$ . Since we have three unknown functions, we use a mixed function space with three function spaces,  $\Phi$ ,  $\eta$  and  $\Psi$ . In the fluid we multiply the momentum equation with  $\Phi$ , the continuity equation with  $\eta$  and the equation for mesh velocity with  $\Psi$  and integrate over the domain in its *current* configuration,  $\Omega^t$ . In the fluid, this yields

$$\frac{\rho_f}{\Delta t}(\mathbf{v}, \Phi)_{\Omega_f} + \rho_f(((\mathbf{v} - \mathbf{w}) \cdot \nabla) \mathbf{v}^{(0)}, \Phi)_{\Omega_f^t} - (p, \nabla \cdot \Phi)_{\Omega_f^t} + 2\mu_f(\epsilon(\mathbf{v}), \nabla \Phi)_{\Omega_f^t} =$$

$$\frac{\rho_f}{\Delta t}(\mathbf{v}^{(1)}, \Phi)_{\Omega_f^t} - (\sigma_f(p, \mathbf{v}) \cdot \mathbf{n}, \Phi)_{\partial \Omega_f^t} - (\sigma_f(p, \mathbf{v}) \cdot \mathbf{n}_f, \Phi)_{\Gamma^t}$$

$$-(\nabla \cdot \mathbf{v}, \eta)_{\Omega_f^t} = 0$$

$$\begin{aligned} \Delta t(\nabla \mathbf{w}, \nabla \Psi)_{\Omega_f^t} &= -(\nabla \mathbf{U}^{(1)}, \nabla \Psi)_{\Omega_f^t} + ([\nabla \mathbf{U}^{(1)} + \Delta t \nabla \mathbf{w}] \cdot \mathbf{n}, \Psi)_{\Omega_f^t} \\ &\quad + ([\nabla \mathbf{U}^{(1)} + \Delta t \nabla \mathbf{w}] \cdot \mathbf{n}_f, \Psi)_{\Gamma^t} \end{aligned}$$

And in the solid

$$\begin{aligned} \frac{\rho_s}{\Delta t}(\mathbf{v}, \Phi)_{\Omega_s} + \Delta t(\sigma_s(\mathbf{v}), \nabla(\Phi))_{\Omega_s} &= \frac{\rho_s}{\Delta t}(\mathbf{v}^{(1)}, \Phi)_{\Omega_s} - (\sigma_s(\mathbf{U}^{(1)}), \nabla \Phi)_{\Omega_s} \\ &\quad - ([\sigma_s(\mathbf{U}^{(1)}) + \Delta t \sigma_s(\mathbf{w})] \cdot \mathbf{n}, \Phi)_{\partial \Omega_s^t} \\ &\quad - ([\sigma_s(\mathbf{U}^{(1)}) + \Delta t \sigma_s(\mathbf{w})] \cdot \mathbf{n}_s, \Phi)_{\Gamma^t} \end{aligned}$$

$$\frac{1}{\delta}(\mathbf{v}, \Psi)_{\Omega_s} - \frac{1}{\delta}(\mathbf{w}, \Psi)_{\Omega_s} = 0$$

The parameter  $\delta$  should be small and ensures the importance of  $\mathbf{v}_s = \mathbf{w}_s$  inside the solid. On the interface, we have distinguished between the normal vector with respect to the fluid and solid domain. In general  $\mathbf{n}_f = -\mathbf{n}_s$ . To be able to set up and assemble the matrices for this system, the equations should be added to form one bilinear form and one linear form.

### 4.3.3 A discussion on functions spaces

We have previously defined the  $L^2$  (def. 4.1) and  $H^1$  (def. 4.2) spaces, as well as the linear continuous galerkin basis functions (section 4.1.2). In order to have a well posed-problem, we need a triple  $(\Phi, \eta, \Psi)$  to satisfy a few given conditions. In the following, a brief justification of the choice of function spaces used in this study are given.

For the incompressible Navier-Stokes equations, much of the mathematical theory and understanding have been developed by investigation of the simplified Stokes flow where the acceleration term is neglected in the momentum equation, that is

$$-\mu \nabla^2 \mathbf{u} + \nabla p = \mathbf{F}$$

Numerous possible pairs  $(\Phi, \eta)$  have been proposed over the years since the first report by Taylor and Hood [22]. The discretization used by Taylor and Hood consists of quadratic piecewise polynomials for the velocity components and linear piecewise polynomials for the pressure and is still a very popular choice of basis functions. These types of elements are often referred to as Taylor-Hood elements or simply just P2-P1 elements.

As mentioned earlier, the final step in the finite element method consists of solving a linear system of equations. In the case of Stokes equations with body forces  $\mathbf{f}$ , a matrix system on the following form needs to be solved

$$\begin{bmatrix} \mathbf{A} & \mathbf{B} \\ \mathbf{B}^T & \mathbf{0} \end{bmatrix} \begin{bmatrix} \mathbf{v} \\ \mathbf{p} \end{bmatrix} = \begin{bmatrix} \mathbf{f} \\ \mathbf{0} \end{bmatrix}$$

Which means that

$$\mathbf{A}\mathbf{v} + \mathbf{B}\mathbf{p} = \mathbf{f} \quad (4.6)$$

$$\mathbf{B}^T \mathbf{v} = \mathbf{0} \quad (4.7)$$

To get an expression for  $\mathbf{v}$ , we multiply (4.6) with  $\mathbf{A}^{-1}$  to obtain

$$\mathbf{v} = \mathbf{A}^{-1}(\mathbf{f} - \mathbf{B}\mathbf{p})$$

And insert this expression into (4.7) to get an equation only involving the pressure

$$\mathbf{B}^T \mathbf{A}^{-1}(\mathbf{f} - \mathbf{B}\mathbf{p}) = \mathbf{0}$$

or

$$\mathbf{B}^T \mathbf{A}^{-1} \mathbf{B} \mathbf{p} = \mathbf{B}^T \mathbf{A}^{-1} \mathbf{f}$$

For the solution to be unique, the matrix  $\mathbf{B}^T \mathbf{A}^{-1} \mathbf{B}$  often referred to as the *Schur complement* needs to be non-singular. A necessary and sufficient condition for this is that  $\text{Ker}(\mathbf{B}) = \{0\}$ , or

$$\sup_{\mathbf{v}_h} \int p_h \nabla \cdot \mathbf{v}_h > 0$$

For all discrete pressures  $p_h \neq 0$ . This ensures solvability. For convergence, the famous Babuska-Brezzi (BB), or inf-sup condition needs to be satisfied [23]

$$\inf_{p_h} \sup_{\mathbf{v}_h} \frac{\int_{\Omega} p_h \nabla \cdot \mathbf{v}_h}{\|\mathbf{v}_h\|_1 \|p_h\|_0} \geq D > 0$$

Where  $D$  is a constant independent of the mesh resolution.

Provided this condition is satisfied the following error estimate should hold for the Stokes equations

$$\|\mathbf{v}_h - \mathbf{v}\|_1 + \|p_h - p\|_0 < C(h^k \|\mathbf{v}\|_{k+1} + h^{l+1} \|p\|_{l+1})$$

Where  $k$  and  $l$  are the degrees of polynomials used for velocity components and pressure, respectively. To obtain optimal convergence for the solution the polynomial degree should be one higher for the velocity components than for the pressure, that is,  $k = l + 1$ . For instance, using P3-P1 elements, computer resources are "wasted" by introducing more degrees of freedom (dofs) without improving convergence. Several choices of element type combinations, for instance Linear elements (P1) both for velocity and pressure do not satisfy the BB condition, and as a consequence unphysical oscillations in pressure can be seen.

Elements not satisfying the BB condition can be used if a proper stabilization is introduced. Due to the drastical reduction in dofs, P1-P1 elements are often used when large systems are solved for instance in commercial software. This combination is default in COMSOL, while for 3D problems in FLUENT, a slightly different element, the "mini-element" is used as first developed by Fortin [24]. This element is linear but with an extra degree of freedom known as a bubble in the center.

In this study, P2-P1 elements are used for the material velocity and pressure. However, a function space is also needed for the domain velocity,  $\mathbf{w}$ . As discussed by Quaini [25], P1-elements for the domain velocity will ensure the transformation of straight lines in the new domain. In the fluid momentum equation, the function  $\mathbf{w}$  is only used in the term  $((\mathbf{v} - \mathbf{w}) \cdot \nabla) \mathbf{v}^{(0)}$  and since  $\mathbf{v}$  is a polynomial of degree 2,  $\mathbf{v} - \mathbf{w}$  will also be a polynomial of degree 2. Therefore, the

#### 4.3.4 Treatment of boundary conditions

In addition to the boundary conditions described in the original benchmark paper from Turek and Hron, homogeneous Dirichlet conditions are prescribed to the mesh displacement velocity on the domain boundary, i.e

$$\mathbf{w} = 0 \text{ on } \partial\Omega_f^t \cup \partial\Omega_s^t$$

Except for the fluid velocity on the outlet, the domain boundaries (not interface) have prescribed Dirichlet conditions on both  $\mathbf{u}$  and  $\mathbf{w}$ . Therefore the test functions  $\Phi$  and  $\Psi$  will be zero on these boundaries.

If we add all the equations in the previous section together, the contributions to the boundary integral on the interface gives:

$$-(\sigma_f(p, \mathbf{v}) \cdot \mathbf{n}_f, \Phi)_{\Gamma^t} - ([\sigma_s(\mathbf{U}^{(1)}) + \Delta t \sigma_s(\mathbf{w})] \cdot \mathbf{n}_s, \Phi)_{\Gamma^t}$$

By leaving this out of the variational form, we weakly impose

$$\sigma_f(p, \mathbf{v}) \cdot \mathbf{n} = \sigma_s(\mathbf{U}) \cdot \mathbf{n}$$

On the interface. The choice of  $\mathbf{n}$  ( $\mathbf{n} = \mathbf{n}_f$  or  $\mathbf{n} = \mathbf{n}_s$ ) is arbitrary, but the same for each side of the equation.

Because we use the same function for fluid velocity and solid velocity, the no-slip condition is naturally incorporated for the fluid on the structure

$$\mathbf{v}_f = \mathbf{v}_s \text{ on } \Gamma^t$$

Because the functions  $\mathbf{v}_f$  and  $\mathbf{v}_s$  share nodes on the interface.

The additional equation for  $\mathbf{w}$  in the fluid also gives rise to boundary conditions on  $\nabla \mathbf{U} \cdot \mathbf{n}$  on the interface. To this end we set

$$\nabla \mathbf{U} \cdot \mathbf{n} = 0$$

and rather let the parameter  $\delta$  underline the importance of  $\mathbf{w} = \mathbf{v}$  *inside* the solid, whereas  $\mathbf{w}$  in the fluid should just ensure a smooth mesh displacement.

On the outlet, we assign the stress-free condition  $\sigma_f(p, \mathbf{v}) \cdot \mathbf{n} = 0$  so the boundary integral also vanish on the outlet for the momentum equation in the fluid.

This means that all integrals involving boundaries will vanish in the variational form. The Dirichlet conditions are imposed in FEniCS as previously described.

### 4.3.5 FSI in FEniCS

There will be some changes and a great leap in complexity compared to the previous example using FEniCS. The main differences and additions are explained here. One thing to highlight is the always ongoing changes and updates in the dolfin library. Therefore, if a solver was to be used by someone other than the writer, it will constantly need updates and fixes. This thesis do not intend to present a solver with great complexity and many options, but rather outline the most important lines of code and explain difficulties behind the FSI problem in FEniCS. The explanation here intends that a reader somewhat familiar with FEniCS should be able to implement such a code within a short amount of time.

The computational mesh is constructed in gmsh with a straight boundary dividing the fluid and the solid. This way, the class `MeshFunction` can be utilized by dividing the mesh in two subdomains. We now assume we have classes describing the solid and fluid region, implemented with functions similiar to the boundary functions in the Poisson example.

```
mesh = Mesh('FSI_mesh.xml')
SD = MeshFunction('uint', mesh, mesh.topology().dim())
SD.set_all(0)
Elastic().mark(SD,1)
```

where

```
class Elastic(SubDomain):
    def inside(self,x, on_bnd):
        # returns True if vector x in solid.
```

'uint' means that the `MeshFunction` has values of nonnegative integers. The last argument ensures the `MeshFunction` to have the same dimension as the mesh.

Using the MeshFunction, the fluid domain have been marked 0, and the solid domain have been marked 1. Integration over the two domains can be separated by passing this number to `dx` in the variational formulation. A similar class, the FacetFunction

```
boundaries = FacetFunction("size_t",mesh)
```

is used to mark the boundaries and, if needed, separate integration over specific parts of the boundary.

'uint' means that the MeshFunction has values of nonnegative integers. 'size\_t' means the same for the FacetFunction. The last argument to MeshFunction ensures the MeshFunction to have the same dimension as the mesh.

We need a function spaces for all three testfunctions, corresponding to `v`, `p` and `w`, and in this case we can use a handy FEniCS class to create a mixed function space. Test -and trial functions should also be created from this mixed space.

```
V = VectorFunctionSpace(mesh,'CG',2)
P = FunctionSpace(mesh,'CG',1)
W = VectorFunctionSpace(mesh,'CG', 1)
VPW = MixedFunctionSpace([V,P,W])
v,p,w = TrialFunctions(VPW)
phi,eta,psi = TestFunctions(VPW)
```

All Dirichlet boundary conditions need to be specified, and the functions need to be in the space of the respective trial function where the condition is set. For instance, the top boundary of the domain have been marked 2 with the FacetFunction, and we want to prescribe the no-slip condition on the fluid velocity.

```
noslip = Constant((0.0,0.0))
bcv2 = DirichletBC(VPW.sub(0),noslip,boundaries,2) # Top
```

All the Dirichlet boundary conditions are put together in a list, `bcs`.

When the Mesh -and FacetFunctions have been properly marked, we need to map the information from these classes to the different measures, `dx`, `ds` and `dS` representing integration over cells, exterior facets and interior facets, respectively. This is done by:

```
dS = Measure('dS')[boundaries]
dx = Measure('dx')[SD]
ds = Measure('ds')[boundaries]

dx_f = dx(0,subdomain_data=SD)
dx_s = dx(1,subdomain_data=SD)
```

The last two lines simplifies the integrands in the variational form and make it more clear which expressions are to be used in the fluid domain and which

should be used in the solid domain.

Sometimes, it can be convenient to define the constants used in FEniCS as instances of the class `Constant`, to avoid re-compiling if the value of the constant is changed. e.g.

```
dt = 0.0003
k = Constant(dt)
```

We can now attention our focus to the variational form. Regular Python functions can be used in the variational formulation, and by defining these two

```
def sigma_s(U):
    return 2*mu_s*sym(grad(U)) + lamda*tr(sym(grad(U)))*Identity(2)

def eps(v):
    return 2*mu_f*sym(grad(v))
```

To be able to start the simulation some initial conditions are needed, and by setting

```
U = Function(W)
v1 = Function(V)
v0 = Function(V)
```

The initial conditions are simply set to be zero both for velocity and displacement.

The variational form is very similar to the mathematics. We define the bilinear and linear forms,  $a$  and  $L$ , for each separate equation, momentum, continuity and the movement of the domain in both the fluid and solid domain (except for continuity in the solid). For instance,  $a_{MF}$  will denote the bilinear form,  $a$ , for the momentum equation in the fluid.

```

# FLUID
aMF = rho_f/k*inner(v,phi)*dx_f + \
       rho_f*inner(grad(v0)*(v-w),phi)*dx_f - \
       inner(p,div(phi))*dx_f + \
       2*mu_f*inner(eps(v),grad(phi))*dx_f

LMF = rho_f/k*inner(v1,phi)*dx_f

aCF = -inner(div(v),eta)*dx_f

aDF = k*inner(grad(w),grad(psi))*dx_f
LDF = -inner(grad(U),grad(psi))*dx_f

aF = aMF + aCF + aDF
LF = LMF + LDF

# SOLID
aMS = rho_s/k*inner(v,phi)*dx_f + \
       k*inner(sigma_s(v),grad(phi))*dx_f

LMS = rho_s/k*inner(v1,phi)*dx_f - \
       inner(sigma_s(U),grad(phi))*dx_f

aDS = 1/delta*inner(u,w)*dx_f - \
       1/delta*inner(d,w)*dx_f

aS = aMS + aDS
LS = LMS

```

We can now add the forms together to obtain one bilinear and one linear form

```

a = aS + aF
L = LS + LF

```

Before the time loop starts we define a function for holding the solution:

```
VPW_ = Function(VPW)
```

This function will consist of all values for  $\mathbf{v}$ ,  $p$  and  $\mathbf{w}$ .

The time loop runs until the current time exceeds the specified end time,  $T$ . The forms change in time, and thus needs to be assembled to be updated to use the correct values for  $\mathbf{v}^{(1)}$ ,  $\mathbf{w}^{(1)}$ ,  $\mathbf{U}^{(1)}$  and  $\mathbf{v}^{(0)}$ . The linear form needs an update each time step, while the bilinear form needs to be updated every single iteration inside the time loop. For the iterative method, we have chosen the Picard iteration based on the simplicity of the algorithm compared to Newton's method, especially when dealing with a mixed function space consisting of three separate spaces. The iteration runs until the  $L^2$  norm of  $(\mathbf{v} - \mathbf{v}^{(0)})$  is less than a given number,  $\tau$ , or if the number of iterations becomes to large.

```

while t < T:
    ...
    b = assemble(L)
    ...
    while error > tau and k_iter < max_iter:
        A = assemble(a)
        A = ident.zeros()
        [bc.apply(A,b) for bc in bcs]
        solve(A,VPW_.vector,b,'lu')
        v_,p_,w_ = VPW_.split(True)
        eps = errornorm(v_,v0,degree_rise=3)
        k_iter += 1

    v0.assign(v_)

```

The second statement within the iteration loop is needed because the lack of an equation for  $p$  within the solid. The `ident.zeros()` function replaces zeros with ones on the diagonal of the matrix block, and the solution vector for  $p$  will be zero inside the solid. In FEniCS, a Function has to be defined over the whole mesh, and adjusting the linear system as described is a way to overcome this issue in the present version of DOLFIN (1.6.0). To assign a new value for  $v_0$ , and later be able to calculate drag and lift, we split the solution vector with the argument `True`. The solver is '`lu`' by default, but in this case it is written explicitly. Iterative solvers are in general way faster, but in this case no Krylov Solver was found to converge.

The next problem to address is how the mesh should be updated. The domain should now move with velocity  $\mathbf{w}$ , so we want to move the mesh with  $\Delta t \mathbf{w}$  from one time step to the next. For the total displacement, the update  $\mathbf{U} = \mathbf{U}^{(1)} + \Delta t \mathbf{w}$  should also be taken into account. The actual update of the mesh is done with the functions `move()` and `bounding_box_tree().build()`

```

w_vector()[:] *= float(k)
U_.vector()[:] += w_vector()[:]
mesh.move(w_)
mesh.bounding_box_tree().build(mesh)

v1.assign(v_)

```

The final line is to update the velocity, so we can move to the next time step. Note that the velocity in both the fluid and the solid is updated by this call.

## 4.4 A Discontinuous Galerkin method

Discontinuous Galerkin (DG) methods is a relatively new tool for CFD simulations. The method itself was developed during the 1970s and has been used increasingly the last few decades. Unlike with the Continuous Galerkin elements, we now allow the solution to be discontinuous, i.e cells do not share nodes

anymore. Instead of solving over the whole domain, we now seek approximate continuous solutions on each cell independently of the others. To this end it is convenient to define the average and jump of a discontinuous variable

$$\{\mathbf{v}\} = \frac{1}{2}(\mathbf{v}^+ + \mathbf{v}^-) \quad [\mathbf{v}] = \mathbf{v}^+ - \mathbf{v}^-$$

where  $\mathbf{v}^+$  and  $\mathbf{v}^-$  is the solution at two neighboring cells at cell  $E^+$  and  $E^-$ . These definitions can be accessed easily in FEniCS as

```
avg(v)
jump(v)
```

The normal vectors are denoted  $\mathbf{n}^+$  and  $\mathbf{n}^-$ . If consistent, the choice of  $\mathbf{n}$  is arbitrary. [26]

#### 4.4.1 Stokes flow

Consider the following problem in  $\Omega = [0, 1] \times [0, 1]$ :

$$\begin{aligned} -\nabla \cdot \sigma &= 0 \text{ in } \Omega \\ \nabla \cdot \mathbf{v} &= 0 \text{ in } \Omega \\ \mathbf{v} &= 0 \text{ on } \Omega_w \\ p\mathbf{n} - \mu \frac{\partial \mathbf{v}}{\partial n} &= p_{in}\mathbf{n} \text{ on } \Omega_{in} \\ p\mathbf{n} - \mu \frac{\partial \mathbf{v}}{\partial n} &= p_{out}\mathbf{n} \text{ on } \Omega_{out} \end{aligned}$$

where  $\sigma$  is the incompressible Newtonian fluid stress tensor as previously described. The inlet is at  $x=0$ , while the outlet is at  $x=1$ . The rigid walls are situated where  $y=0$  and  $y=1$ . By choosing  $p_{in} = 2$ ,  $p_{out} = 0$ , a steady Poiseuille flow should be obtained. The boundary condition on the inlet and outlet are Pseudo-traction as described in chapter 3.

By integrating Stokes equation by parts, adding symmetry and penalty terms as in [27] we end up with a consistent DG-method. Since the method involves many terms we derive the weak formulation term by term. The set of all elements are denoted as  $e$ , interior facets as  $\Gamma$  and exterior facets as  $\partial\Omega$ . Starting with the diffusion term in divergence form, we multiply with a test function and integrate by parts:

$$\begin{aligned} 2\mu \sum_{E \in e} (\epsilon(\mathbf{v}), \epsilon(\Phi))_E - 2\mu \sum_{E \in \Gamma} (\{\epsilon(\mathbf{v})\} \cdot \mathbf{n}_e, [\nabla \Phi])_E - 2\mu \sum_{E \in \Gamma} (\{\epsilon(\Phi)\} \cdot \mathbf{n}_e, [\nabla \mathbf{v}])_E \\ + \frac{\beta}{h} \sum_{E \in \Gamma} ([\mathbf{v}], [\Phi])_E - 2\mu \sum_{E \in \partial\Omega} (\Phi, \epsilon(\mathbf{v}) \cdot \mathbf{n}_e)_E \\ - 2\mu \sum_{E \in \partial\Omega} (\mathbf{v}, \epsilon(\Phi) \cdot \mathbf{n}_e)_E + \frac{\beta}{h} \sum_{E \in \partial\Omega} (\mathbf{v}, \Phi)_E \end{aligned}$$

Similarly, the contributions from the term  $-\nabla p$  will be

$$-\sum_{E \in e} (p, \nabla \cdot \Phi)_E + \sum_{E \in \Gamma} (\{p\}, [\Phi] \cdot \mathbf{n}) + \sum_{E \in \Gamma} (\{\eta\}, [\mathbf{v}] \cdot \mathbf{n})$$

With  $DG_1 \times DG_0$  elements for velocity and pressure the following results were obtained with the convergence rate computed as

$$\frac{\ln(\frac{e^{n+1}}{e^n})}{\ln(\frac{h^{n+1}}{h^n})},$$

$N$  representing the number of cells in the  $N \times N$  unit square and  $h$  computed in FEniCS as `mesh.hmin()` for each refinement

N	dofs	$\ v - v_h\ _{L^2}$	$\ p - p_h\ _{L^2}$	rate u	rate p
4	224	1.8318e-02	1.5590e-01	—	—
8	896	1.0732e-02	7.6566e-02	0.7713	1.0259
16	3584	5.8110e-03	3.7890e-02	0.8851	1.0149
32	14336	3.0221e-03	1.8895e-02	0.9432	1.0038
64	57344	1.5410e-03	9.4481e-03	0.9717	0.9999
128	229376	7.7808e-04	4.7267e-03	0.9859	0.9992

## 4.5 Womersley Flow

In the cardiovascular system, pressure pulses travel along different blood vessels such as veins, capillaries and the aorta. These types of pulsating flows have been given the name Womersley flow. The characteristics and velocity profile of the flow depends of several parameters such as the length of the tube or channel, pulsation frequency and fluid properties. In the end, the ratio between transient inertial forces and viscous forces is the fundamental difference separating flow patterns in pulsating flow. To this end the Womersley number,  $\alpha$  is defined as follows:

$$\alpha = \frac{\text{transient inertial force}}{\text{viscous force}} = \frac{\rho \omega V}{\mu V L^{-2}} = \frac{L^2 \omega \rho}{\mu}$$

Where,  $\rho$  is the fluid density,  $\mu$  is the dynamic viscosity,  $L$  is a length scale and  $\omega$  is the pulsation frequency. In the 2D-model presented here, the modeling of SAS around the spinal cord consists of two channels where the Womersley number

$$\alpha = L \left( \frac{\omega \rho}{\mu} \right)^{\frac{1}{2}}$$

Would have a large impact on the flow characteristics. A low Womersley number (typically  $\alpha < 1$  means the frequency is relatively low so the flow develops a velocity profile close to a parabola at each cycle. When  $\alpha$  is large ( $\alpha > 10$ ) the inertial forces dominate and more complicated phenomena such as bidirectional flow, i.e. flow in opposite directions over a cross section, could occur.

Pulsating flow tends to give rise to some horizontal or radial flow with the boundary conditions previously described. We will return to this issue in the next subsection. In the analytical solution to these kinds of problems, no such velocity components exists due to the assumption on axial flow only at the inlet and outlet, that is, the following conditions should hold

$$\begin{aligned}\mathbf{v} \cdot \boldsymbol{\tau} &= 0 \text{ on } \partial\Omega_{\text{in}} \\ \mathbf{v} \cdot \boldsymbol{\tau} &= 0 \text{ on } \partial\Omega_{\text{out}}\end{aligned}\quad (4.8)$$

Where  $\boldsymbol{\tau}$  is the tangential vector on the boundary surface.

The problem consists of solving

$$\begin{aligned}\frac{\partial \mathbf{v}}{\partial t} + (\mathbf{v} \cdot \nabla) \mathbf{v} &= -\nabla \cdot \boldsymbol{\sigma} && \text{in } \Omega \\ \nabla \cdot \mathbf{u} &= 0 && \text{in } \Omega \\ \mathbf{v} &= 0 && \text{on } \Omega_w \\ p &= p_{\text{in}}(t) \text{ and } \mathbf{v} \cdot \boldsymbol{\tau} = 0 && \text{on } \Omega_{\text{in}} \\ p &= p_{\text{out}}(t) \text{ and } \mathbf{v} \cdot \boldsymbol{\tau} = 0 && \text{on } \Omega_{\text{out}}\end{aligned}$$

Exact solutions exists to both the channel and pipe cases. Langlois and Deville [28] have derived several solutions to equations of viscous flow, including channel flow with a pulsatile pressure gradient as above. We now add a oscillating pressure gradient so that

$$-\frac{1}{\rho} \frac{\partial p}{\partial x} = -C \cos(\omega t)$$

$$h = 4$$

$$p = C \cos(\omega t) \boxed{\quad} p = 0$$

$$l = 60$$

Figure 4.8: Schematic of Womersley flow with dimensions as in the spinal cord

where  $C$  is a constant describing the strength of the pulse. Due to the assumption of axial flow only, the momentum equation in  $x$ -direction gives:

$$\frac{\partial v_1}{\partial t} = -\frac{1}{\rho} \frac{\partial p}{\partial x_1} + \nu \frac{\partial^2 v_1}{\partial x_2^2} \quad (4.9)$$

The presented solution did not correspond to the simulations at all, therefore an opportunity to utilize the symbolic python package sympy arised. The solution presented by Langlois and Deville was

$$v_1 = -\frac{C}{\omega} \left[ \left( 1 - \frac{f_1(\omega, x_3)}{f_3(kh)} \right) \sin(\omega t) - \frac{f_2(\omega, x_3)}{f_3(kh)} \cos(\omega t) \right]$$

where

$$\begin{aligned}
 k &= \sqrt{\frac{\omega}{2\nu}} \\
 cc(x) &= \cos(x) \cosh(x) \\
 ss(x) &= \sin(x) \sinh(x) \\
 f_1(\omega, x_3) &= cc(kx_3)cc(kh) + ss(kx_3)ss(kh) \\
 f_2(\omega, x_3) &= cc(kx_3)ss(kh) - ss(kx_3)cc(kh) \\
 f_3(\omega) &= cc^2(\omega) + ss^2(\omega)
 \end{aligned}$$

In sympy, even a complicated solution like this is easy to verify. The package lets the user define symbols to work with. Regular multiplication and general python functions can also be used.

```

from sympy import *
x3, C, x, h, t, w, nu = symbols('x3 C x h t w nu')
k = sqrt(w/(2*nu))
def cc(x):
    return cos(x)*cosh(x)
.
.
.

f3 = cc(w)**2 + ss(w)**2

u = -C/w*((1-f1/f3)*sin(w*t) - f2/f3*cos(w*t))    # presented solution
d2u = nu*diff(diff(u,x3),x3)
dt = diff(u,t)

print simplify(d2u-dt)

```

From (4.9) the code snippet should print the pressure gradient divided by the density

$$\frac{1}{\rho} \frac{\partial p}{\partial x_3} = C \cos(\omega t)$$

This was not the case. Some error with the sign of the solution must have been made.

The solution

$$v_1 = -\frac{C}{\omega} \left[ \left( 1 - \frac{f_1(\omega, x_3)}{f_3(kh)} \right) \sin(\omega t) + \frac{f_2(\omega, x_3)}{f_3(kh)} \cos(\omega t) \right]$$

Where the sign before the cos-term has been changed, yielded the correct pressure gradient, and hence this solution was used when error-estimates were investigated.

### 4.5.1 A penalty method for the boundary conditions

To understand the problems arising with Neumann Conditions on both inlet and outlet we first consider the convection-diffusion equation.

$$\begin{aligned} -\mu \nabla^2 u + \mathbf{v} \cdot \nabla u &= f \quad \text{in } \Omega \\ u &= u_0 \quad \text{on } \partial\Omega_D \\ \mu \frac{\partial u}{\partial n} &= g \quad \text{on } \partial\Omega_N \end{aligned}$$

Where  $u$  is an unknown function,  $\mathbf{v}$  is a prescribed velocity,  $\mu$  is a diffusion constant and  $f$  is a source term. The weak formulation reads:

$$\text{Find } u \in H_{u_0}^1$$

$$\mu(\nabla u, \nabla \phi)_\Omega + (\mathbf{v} \cdot \nabla u, \phi)_\Omega = (f, \phi)_\Omega + (g, \phi)_{\partial\Omega_N} \quad \text{for all } \phi \in H_0^1.$$

Where the subscript on the two H-spaces indicate the values for functions on  $\partial\Omega_D$  for these spaces.

What has not been mentioned so far is the existence and uniqueness of the finite element solutions. To establish some concepts addressing these questions we let  $V$  denote a function space (in particular,  $V$  is a Hilbert space which has to satisfy given conditions on the associated inner product), and the inner product is denoted  $(\cdot, \cdot)_V$  and the norm  $\|\cdot\|_V$ , (see e.g. Elman et al [29]) and define the following

**Definition 4.3 (Coercivity)**

A bilinear form  $a(\cdot, \cdot)$  is said to be coercive with respect to the norm  $\|\cdot\|_V$  if there is a positive constant  $\gamma$  such that

$$a(u, u) \geq \gamma \|u\|_V^2 \quad \text{for all } u \in V$$

**Definition 4.4 (Continuity)**

A bilinear form  $a(\cdot, \cdot)$  is continuous with respect to the norm  $\|\cdot\|_V$  if there is a positive constant  $\Gamma$  such that

$$a(u, u) \leq \Gamma \|u\|_V \|\phi\|_V \quad \text{for all } u, \phi \in V$$

A linear functional  $L(\phi)$  is continuous with respect to  $\|\cdot\|_V$  if there is a constant  $\Lambda$  such that

$$L(\phi) \leq \Gamma \|\phi\|_V \quad \text{for all } \phi \in V$$

In order to have a well posed problem, and ensure the existence of a unique solution  $u \in V$  satisfying

$$a(u, \phi) = L(\phi) \quad \text{for all } \phi \in V$$

$a(\cdot, \cdot)$  and  $L(\cdot)$  have to satisfy these criteria. This is commonly known as the Lax-Milgram lemma.

The convection term

$$c(u, \phi) = (\mathbf{v} \cdot \nabla u, \phi)_\Omega \tag{4.10}$$

makes this problem very different from the Poission-problem (4.1),(4.2), (4.3), used when introducing the finite element method. In the light of the previous definitions we apply Green's theorem to (4.10)

$$\begin{aligned} c(u, \phi) &= \int_{\Omega} \phi \mathbf{v} \cdot \nabla u dx \\ &= - \int_{\Omega} u \mathbf{v} \cdot \nabla \phi dx - \int_{\Omega} u \phi \nabla \cdot \mathbf{v} dx + \int_{\partial\Omega_N} u \phi \mathbf{v} \cdot \mathbf{n} dS \\ &= -c(\phi, u) + \int_{\partial\Omega_N} u \phi \mathbf{v} \cdot \mathbf{n} dS \end{aligned}$$

Where the last step follows from the assumption of incompressibility. From this

$$c(u, u) = \frac{1}{2} \int_{\Omega_N} u^2 \mathbf{v} \cdot \mathbf{n} dS$$

It is obvious that a Neumann condition on the inflow boundary, where  $\mathbf{v}$  and  $\mathbf{n}$  points in opposite directions, makes a negative contribution to the bilinear form  $a(u, u)$ . Therefore coercivity can not be completely ensured, and it typically depends on the magnitude of the velocity at the inlet.

In several problems, prescribing Neumann conditions are simpler than providing inlet velocities. The pressure is set as a scalar value and can be assumed to have no spatial variation over the boundaries if the model has flat surfaces with normals aligned with the longitudinal axis on the inlet and outlet.

Barth and Carey [30] have described a penalty method for imposing the boundary conditions (4.8). This was needed as horizontal flow at, and close to the boundaries caused problems interacting with the elastic spinal cord. The penalty method consists of adding a term at the relevant boundaries, penalizing parts where the boundary condition do not hold. For the velocity, we want  $\mathbf{v} - (\mathbf{v} \cdot \mathbf{n})\mathbf{n}$  on the boundary, therefore the first variation of the least squares penalty functional is added to the original variational formulation

$$I(\mathbf{v}) = \frac{1}{2\epsilon} \int_{\partial\Omega_p} [\mathbf{v} - (\mathbf{v} \cdot \mathbf{n})\mathbf{n}] \cdot [\mathbf{v} - (\mathbf{v} \cdot \mathbf{n})\mathbf{n}] dS$$

where  $0 < \epsilon \ll 1$  is the penalty parameter. The contribution from the first variation will be

$$I'(\mathbf{v})(\Phi) = \frac{1}{\epsilon} \int_{\partial\Omega_p} [\mathbf{v} - (\mathbf{v} \cdot \mathbf{n})\mathbf{n}] \cdot [\Phi - (\Phi \cdot \mathbf{n})\mathbf{n}] dS$$

This term will clearly contribute positively to the bilinear form and the penalty parameter should ensure that this contribution is large. The method is tested on the coupled CFD solver, first with one time step of the Backwards Scheme and gradually refinement of the rectangular mesh. The time step is small, so the error introduced by the time discretization is negligible.

C = 1000

dt = 0.001

T = 0.1

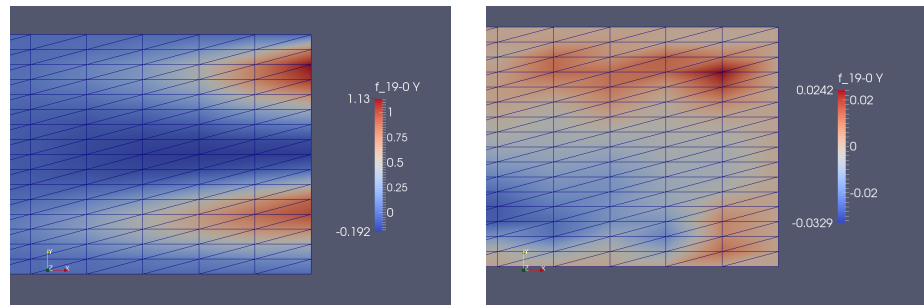
Backward Euler 1st order

N	dofs	$\ v - v_h\ _{L^2}$	rate	$\ v - v_h\ _{H^1}$	rate
4	187	1.00e+00	—	6.65e+00	—
8	659	1.50e-01	2.739	1.95e+00	1.768
16	2467	1.91e-02	2.977	4.95e-01	1.981
32	9539	2.39e-03	2.997	1.24e-01	1.997
64	37507	2.99e-04	2.998	3.10e-02	1.999

Table 4.11: Errors P2-P1 elements

N	dofs	$\ v - v_h\ _{L^2}$	rate	$\ v - v_h\ _{H^1}$	rate
4	419	1.42e+01	—	1.43e+02	—
8	1539	7.84e-01	4.180	1.57e+01	3.186
16	5891	4.75e-02	4.045	1.90e+00	3.047
32	23043	2.97e-03	3.999	2.38e-01	3.000
64	91139	1.86e-04	3.999	2.97e-02	2.999

Table 4.12: Errors P3-P2 elements

Figure 4.9: Velocity distribution in y-direction at  $t=0.1$  without (left) and with the penalty method at the outlet. These velocities are of several orders lower than in the x-direction, but accumulates over time without the penalty method

## Chapter 5

# Material parameters

In the simulations the units millimeters and grams are used. This combination gives back the SI-unit  $\frac{N}{m^2} = \frac{kg \cdot m}{s^2 \cdot m^2} = \frac{g}{s^2 \cdot mm} = Pa$  for pressure, and is also convenient when considering the scale of the spinal cord. CSF is modeled as water at  $37^\circ C$ , i.e  $\rho_f = 10^{-3} \frac{g}{mm^3}$  and  $\nu_f = 0.658 \frac{mm^2}{s}$ .

For the spinal cord, studies have shown a huge variety in material parameters. One of the most measured properties in the mammalian central nervous system is probably the Young's modulus,  $E$  according to Smith, Humphrey [31]. In addition to this, values for the Poisson ratio,  $\nu_P$  needs to be found. In the literature, there is a huge gap in reported Young's modulus for spinal cord tissue.

Article	Region	Model	Parameters
Hung et al. [32]	spinal cord	Experimental	$E = 0.26 \text{ MPa}$
Ben-Hatira et al. [33]	spinal cord	Nonlinear elastic	$E = 1.4 \text{ MPa}$ $\nu = 0.499$
Ozawa et al. [34]	spinal cord	Experimental	$E = 16 \text{ kPa}$
Smith and Humphrey [31]	spinal cord	Experimental	$E = 5.0 \text{ kPa}$ $\nu = 0.479$
Cheng et al. [35]	spinal cord	Review	$E = 0.0119-1.98 \text{ MPa}$
Clarke [36]	spinal cord	Review	$E = 0.012-1.37 \text{ MPa}$
Persson et al. [37]	spinal cord	Review (linear elastic)	$E = 0.26-1.3 \text{ MPa}$

Table 5.1: Summary of elastic parameters used in literature (as presented in Klystad [2])

Smith and Huphrey used the following values for these parameters.

$$E = 5 * 10^4 \text{ dyn/cm}^2 = 5000 \text{ Pa}$$

$$\nu_P = 0.479$$

From this, Lame's parameters for the spinal cord were determined as

$$\mu_s = \frac{E}{2(1 + \nu_P)} = 1.7 \cdot 10^3 \text{ Pa}$$

$$\lambda_s = \frac{\nu_P E}{(1 + \nu_P)(1 - 2\nu_P)} = 3.9 \cdot 10^4 \text{ Pa}$$

The permeability,  $\kappa$  is used as a measurement for the how fluid flows in a porous medium. A large permeability indicates a pervious medium. We use the value from [Karen, Ida]

$$\kappa = 1.4 \cdot 10^{-15} \text{ m}^2$$

# Chapter 6

## Simulating interaction between CSF and the Spinal Cord

The previously described model is used on a different geometry based on idealized versions of the spinal cord. The meshes have the same dimensions as found in previous work by Drøsdal, [3] except for the size of the syrinx which is increased from 1 mm to 3 mm in diameter.

### 6.1 Overview of previous studies

To our knowledge, few studies has investigated fluid-structure interaction modeling of the CSF and the spinal cord including a syrinx. The spinal cord has fibres oriented in the axial direction and a direction-dependent Youngs modulus would then be expected.

In the literature values range between 0.012 to 1.98 MPa. As reported by [36] most of spinal cord experimental studies use a tensile test, and the stress-strain and stress-relaxation responses of the spinal cord are non-linear. Therefore, it will in general be hard to compare results from different studies using different arbitrary levels of strain. Another approach used by Kwon [38], focuses more on spinal cord injuries and are thus more interested in properties during compression. From the modeling point of view, both approaches is of interest, and better constitutive models could be attained by combining results from several of these studies. In this work, however, we limit Youngs modulus to be a constant independent of spatial direction. Such an assumption has been made in all the previous cited works in this thesis.

Some studies have investigated the effects of FSI on the spinal cord movement and CSF pressure in geometries without a syrinx. Clark [39] assumed the Youngs modulus to be 1 MPa for the spinal cord, and in their initial tests

this choice caused only small displacements. Therefore the conclusion was that FSI had a negligible effect on CSF pressure in the SAS.

Cheng et al. [40] investigated FSI effects on a patient-specific 3D-geometry. In their model they assumed a Youngs modulus of 0.7 MPa, and reached the same conclusion as Clark. As highlighted: *"This study informs that fluid structure interaction has no effect on CSF pressure"*.

Clearly, a too high elastic modulus will undermine the effects of FSI, if they do exist. Considering the wide range of material parameters reported in the literature for the spinal cord, we believe further investigation is necessary to be able to make such a statement. In addition, these two studies does not seem to investigate syringomelia as a primary target, and therefore important effects of FSI could have been overlooked in these specific cases.

In porous models presented by Drøsdal, [3] fluid pressure within the cord was altered by the presence of a syrinx but the CSF pressure in the SAS was not. velocities up to only 3e-7 cm/s inside the syrinx was reported, and therefore there must be some other effects causing the more rapid fluid movement inside the syrinx.

To our knowledge, the most noted group working on FSI effects on Syringomelia include the group of Chris D. Bertram at the University of Sydney. Some of their work include research on pressure waves propagating in the spinal cord in the presence of a syrinx [41],[42],[43]. Even though, in this specific paper Bertram focuses on the overlap between the cervical and thoracic segments of the spinal cord, the mechanisms of interest remians the same,

xxx Move to medical section? xxx namely the 'slosh' mechanism proposed by Williams in 1980 [44]. In this theory, increased CSF pressure in the SAS is transmitted to the syrinx generating waves along the walls. Compression of the upper part of the syrinx results in a downwards displacement of the lower part resulting in enlargement of the syrinx.

Even with today's high quality magnetic resonance imaging, (MRI) or phase contrast MR (PC-MR), exact velocities are hard to measure. Healthy subjects also has very complex CSF flow and thus difficult to observe or quantify. Since the Chiari I malformation is associated with abnormal CSF flow, a realistic model simulating the pre-operative case needs abnormal inflow or pressure boundary conditions. The latter is extremely hard to measure exact.

### 6.1.1 Pressure measurements in patients with syringomelia

Williams (1981) [45] and Häck (2001) [46] investigated the pressure gradient between the intracranial and spinal (lumbar) CSF compartments. In their work the pulsatile pressure were not analyzed, which seem to be more reliable in predicting intracranial compliance according to more recent studies by Eide [47, 48, 49, 50]. Frič and Eide also measured the pulsatile pressure gradient between the two compartments and have found significantly higher (mean wave amplitude, MWA) gradients in patients with evidence of syringomyelia (12/26 patients) than in those without. ( $3.7 \pm 2.0$  mmHg vs  $2.1 \pm 1.3$  mmHg;  $p = 0.02$ )

[51]. See figure 6.1 for a graphical representation.

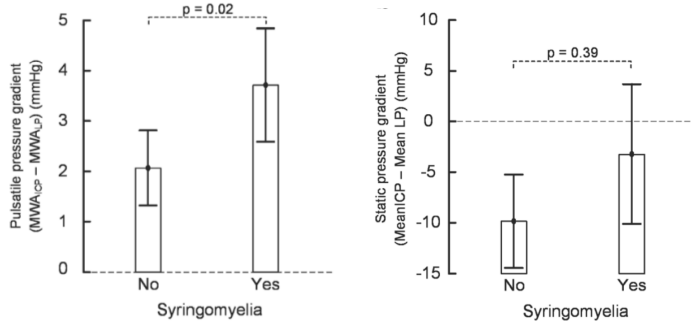


Figure 6.1: Pulsatile (left) and static pressure gradient in patients as used in the study by Frič and Eide [51]

The pulsatile intracranial pressure (ICP) as well as pulsatile pressure gradients were clearly abnormal or with borderline values in 69 and 71 % of Chiari I patients, respectively. Without any further speculation, it is interesting to note that these numbers are very close to the number of Chiari I patients that develops a syrinx. The median pressure difference in patients with abnormal pressure gradient were 2.6 mm Hg between the intracranial CSF pressure and the lumbar CSF pressure. The actual mean static ICP was measured to a median of 7.1 mmHg for the patients (range -0.7 – 13.0), whereas the median of the mean lumbar pressure LP in the patients were 15.1 mm Hg. Czosnyka and Pickard [52] reported ICP for healthy adult subjects to be 7 – 15 mm Hg. Williams [53] measured pressure up to 70 mm Hg and 97 mmHg in the SAS in the cisternal (just below the cerebellum) and lumbar region, respectively during coughing. Sansur et al. [54] measured the SAS pressure at the L5-level and found pressures up to 125 mm Hg in patients coughing. The baseline pressures for healthy subjects were reported to be 8.6 – 13.4 mm Hg.

From the modeling point of view, these measurements are of high interest in prescribing the correct boundary conditions at the top and bottom of the cord and SAS model. There are some challenges however. (Discuss pressure measurements in [51], pressure is always higher in lumbar than in Intracranial)

(Comment on experiments by Martin et al. [55])

## 6.2 Assessment of CSF velocities before and after decompression surgery

We hypothesized that FSI-effects (deformation and pressure wave propagation) was at least partially responsible for the flow up to 3 cm/s within the syrinx

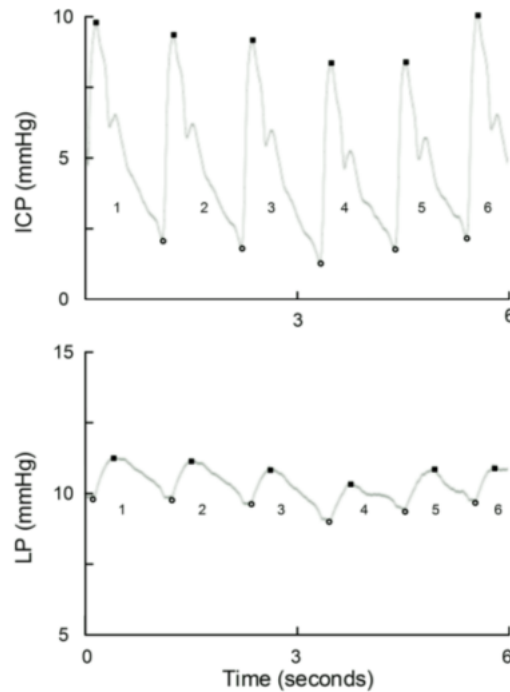


Figure 6.2: Intracranial (ICP) and lumbar (LP) pressure measured simultaneously by Frič and Eide

as reported by Brucker and Haughton in an assessment of CSF velocities and Cord Motion Before and After Chiari 1 Decompression. The study focused on the upper region (C1-C5) of the spinal cord.

xxx ALSO READ 5, 13, 21, 45 from Karen xxx

CSF flow was measured with PCMR on three different stages: Pre-operative, 2 months post-operative and 10 months post-operative when the patient had no remaining symptoms. (Add (weighted?) velocity profiles)

### 6.3 Linear Results

For all Spinal Cord simulations we apply pressure boundary conditions on the inlet and outlet as described under Womersley Flow in chapter 4. First, a sinusoidal varying pressure was applied to the boundaries with a maximum of 20 Pa difference between top and bottom. This applied pressure gradient has previously been reported to result in peak velocities of around 6 cm/s assuming a rigid, but porous cord. [3] The Simulations were run 10 cycles where a steady state was reached. Quantities of interest are the peak velocity in the SAS,  $\max|\mathbf{v}|$ , the peak velocity inside the syrinx in the spinal canal,  $\max|\mathbf{v}_{sc}|$  and the maximum displacement  $\max|\mathbf{U}|$  in both x- and y-direction.

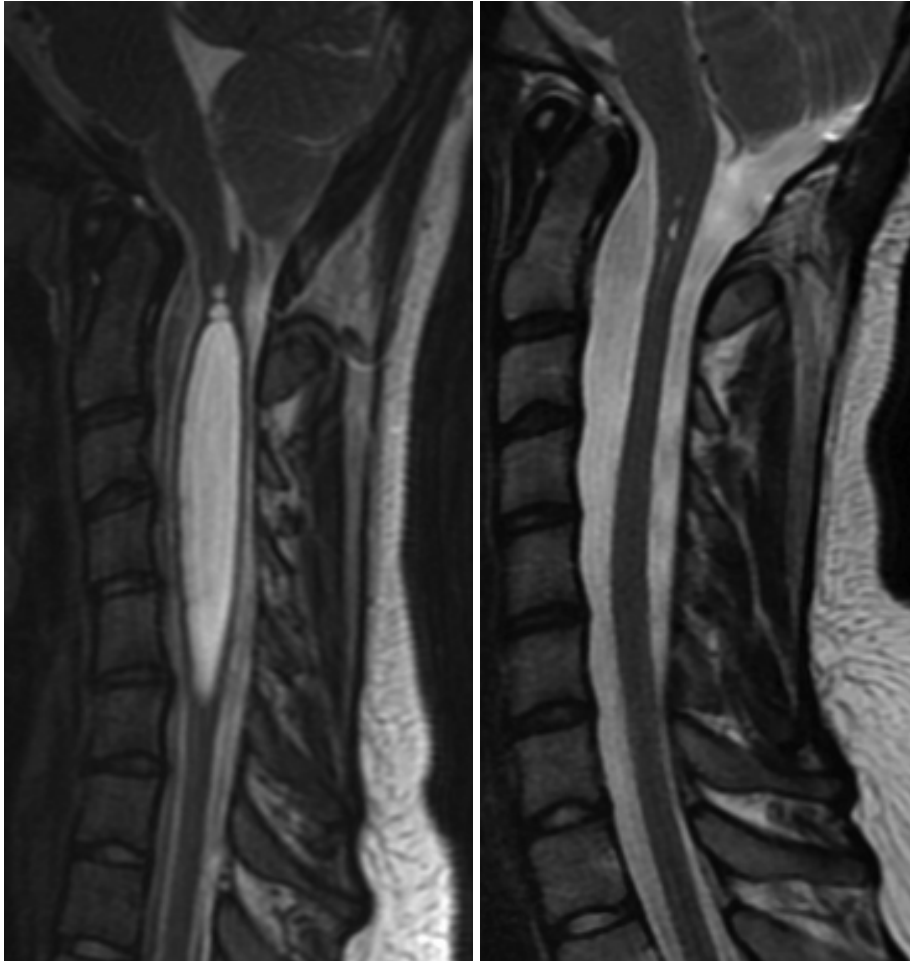


Figure 6.3: MRI image of 14 year old female subject before and 10 months after decompression. Note the withdrawal of the cerebellar tonsils in the post-operative image on the right

$N_x$	$N_y$	dofs	$\max \mathbf{v} $ [cm/s]	$\max \mathbf{v}_{sc} $ [cm/s]	$\max \mathbf{U}_x $ [mm]	$\max \mathbf{U}_y $ [mm]
18	30	6281	6.11	0.79	0.34	0.07
36	60	24437	6.02	0.83	0.33	0.02

Table 6.1:  $E = 16kPa$ ,  $\Delta t = 0.002s$ ,  $T = 10$ ,  $\rho_s = 2\rho_f$

$N_x$	$N_y$	dofs	$\max \mathbf{v} $ [cm/s]	$\max \mathbf{v}_{sc} $ [cm/s]	$\max \mathbf{U}_x $ [mm]	$\max \mathbf{U}_y $ [mm]
18	30	6281	7.75	2.30	1.30	0.16

Table 6.2:  $E = 5kPa$ ,  $\Delta t = 0.002s$ ,  $T = 10s$ ,  $\rho_s = 2\rho_f$

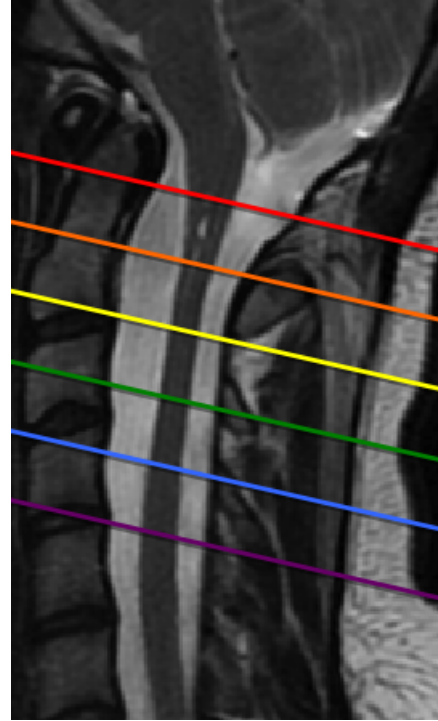


Figure 6.4: Levels C1-C2, C2, C2-C3, C3, C3-C4 and C4-C5

## 6.4 Nonlinear Results

New simulations. Non-linear addition in both  $\sigma$  and convection.  $\rho_s = 1.75\rho_f$   
Else, same

$N_x$	$N_y$	dofs	$\max \mathbf{v} $ [cm/s]	$\max \mathbf{v}_{sc} $ [cm/s]	$\max \mathbf{U}_x $ [mm]	$\max \mathbf{U}_y $ [mm]
18	30	6281	7.10	2.28	0.96	0.06
36	60	24437	6.71	2.07	0.86	0.06

Table 6.3:  $E = 5kPa, \Delta t = 0.002s, T = 10s, \rho_s = 1.75\rho_f$ 

$N_x$	$N_y$	dofs	$\max \mathbf{v} $ [cm/s]	$\max \mathbf{v}_{sc} $ [cm/s]	$\max \mathbf{U}_x $ [mm]	$\max \mathbf{U}_y $ [mm]
18	30	6281	5.93	0.96	0.35	0.02

Table 6.4:  $E = 16kPa, \Delta t = 0.002s, T = 10, \rho_s = 2\rho_f$

# Bibliography

- [1] K.-H. Støverud, “Relation between the chiari i malformation and syringomyelia from a mechanical perspective,” 2014.
- [2] N. K. Kylstad, “Simulating the viscoelastic response of the spinal cord,” 2014.
- [3] I. N. Drøsdal, “Porous and viscous modeling of cerebrospinal fluid flow in the spinal canal associated with syringomyelia,” 2011.
- [4] D. Van Wyngaerde, C. R. Noback, and R. Carola, *Human anatomy and physiology*. McGraw-Hill College, 1995.
- [5] M. F. Quigley, B. Iskandar, M. A. Quigley, M. Nicosia, and V. Haughton, “Cerebrospinal fluid flow in foramen magnum: temporal and spatial patterns at mr imaging in volunteers and in patients with chiari i malformation 1,” *Radiology*, vol. 232, no. 1, pp. 229–236, 2004.
- [6] A. Thompson, N. Madan, J. Hesselink, G. Weinstein, A. M. del Rio, and V. Haughton, “The cervical spinal canal tapers differently in patients with chiari i with and without syringomyelia,” *American Journal of Neuroradiology*, 2015.
- [7] O. Reynolds, *Papers on Mechanical and Physical Subjects, The Sub-Mechanics of the Universe*, vol. 3. Cambridge University Press, Cambridge, 1903.
- [8] F. White, *Viscous Fluid Flow*. McGraw-Hill series in mechanical engineering, McGraw-Hill, 3 ed., 2006.
- [9] J. N. Newman, *Marine Hydrodynamics*. The MIT Press, 1977.
- [10] P. K. Kundu, I. M. Cohen, and D. R. Dowling, *Fluid Mechanics*. Elsevier, Academic Press, 5 ed., 2012.
- [11] H. F. Wang, *Theory of linear poroelasticity*. 2000.
- [12] D. A. Nield and A. Bejan, *Convection in Porous Media*. Springer, 4 ed., 2013.
- [13] J. Donea, A. Huerta, J.-P. Ponthot, and A. Rodriguez-Ferran, *Encyclopedia of Computational Mechanics Vol. 1: Fundamentals., Chapter 14: Arbitrary Lagrangian-Eulerian Methods*. Wiley & Sons, 2004.

- [14] A. M. Winslow, ““equipotential” zoning of two-dimensional meshes,” tech. rep., California Univ., Livermore (USA). Lawrence Livermore Lab., 1963.
- [15] H. P. Langtangen, *Finite Element Method*. 2015.
- [16] S. Brenner and R. Scott, *The mathematical theory of finite element methods*, vol. 15. Springer Science & Business Media, 2007.
- [17] M. Schäfer, S. Turek, F. Durst, E. Krause, and R. Rannacher, *Benchmark computations of laminar flow around a cylinder*. Springer, 1996.
- [18] S. Turek and J. Hron, *Proposal for numerical benchmarking of fluid-structure interaction between an elastic object and laminar incompressible flow*. Springer, 2006.
- [19] A. Y. Tang and N. Amin, “Some numerical approaches to solve fluid structure interaction problems in blood flow,” in *Abstract and Applied Analysis*, vol. 2014, Hindawi Publishing Corporation, 2014.
- [20] J. Hron and S. Turek, *A monolithic FEM/multigrid solver for an ALE formulation of fluid-structure interaction with applications in biomechanics*. Springer, 2006.
- [21] K. Selim, “Adaptive finite element methods for fluidstructure interaction and incompressible flow,” 2011.
- [22] C. Taylor and P. Hood, “A numerical solution of the navier-stokes equations using the finite element technique,” *Computers & Fluids*, vol. 1, no. 1, pp. 73–100, 1973.
- [23] F. Brezzi and M. Fortin, *Mixed and hybrid finite element methods*, vol. 15. Springer Science & Business Media, 2012.
- [24] M. Fortin, “Old and new finite elements for incompressible flows,” *International Journal for numerical methods in fluids*, vol. 1, no. 4, pp. 347–364, 1981.
- [25] A. Quaini, “Algorithms for fluid-structure interaction problems arising in hemodynamics,” 2009.
- [26] B. Rivière, *Discontinuous Galerkin methods for solving elliptic and parabolic equations: theory and implementation*. Society for Industrial and Applied Mathematics, 2008.
- [27] B. Rivière and I. Yotov, “Locally conservative coupling of stokes and darcy flows,” *SIAM Journal on Numerical Analysis*, vol. 42, no. 5, pp. 1959–1977, 2005.
- [28] W. E. Langlois and M. O. Deville, *Slow viscous flow*. Springer, 1964.
- [29] H. C. Elman, D. J. Silvester, and A. J. Wathen, *Finite elements and fast iterative solvers: with applications in incompressible fluid dynamics*. Oxford University Press (UK), 2014.

- [30] W. L. Barth and G. F. Carey, “On a boundary condition for pressure-driven laminar flow of incompressible fluids,” *International journal for numerical methods in fluids*, vol. 54, no. 11, pp. 1313–1325, 2007.
- [31] J. H. Smith and J. A. Humphrey, “Interstitial transport and transvascular fluid exchange during infusion into brain and tumor tissue,” *Microvascular research*, vol. 73, no. 1, pp. 58–73, 2007.
- [32] T.-K. Hung, G.-L. Chang, H.-S. Lin, F. R. Walter, and L. Bunegin, “Stress-strain relationship of the spinal cord of anesthetized cats,” *Journal of biomechanics*, vol. 14, no. 4, pp. 269–276, 1981.
- [33] F. Ben-Hatira, K. Saidane, and A. Mrabet, “A finite element modeling of the human lumbar unit including the spinal cord,” *Journal of Biomedical Science and Engineering*, vol. 5, no. 3, p. 150, 2012.
- [34] H. Ozawa, T. Matsumoto, T. Ohashi, M. Sato, and S. Kokubun, “Mechanical properties and function of the spinal pia mater,” *Journal of Neurosurgery*, vol. 1, no. 1, pp. 122–127, 2004.
- [35] S. Cheng, E. C. Clarke, and L. E. Bilston, “Rheological properties of the tissues of the central nervous system: a review,” *Medical engineering & physics*, vol. 30, no. 10, pp. 1318–1337, 2008.
- [36] E. C. Clarke, “Spinal cord mechanical properties,” in *Neural Tissue Biomechanics*, pp. 25–40, Springer, 2010.
- [37] C. Persson, J. L. Summers, and R. M. Hall, “Modelling of spinal cord biomechanics: In vitro and computational approaches,” in *Neural Tissue Biomechanics*, pp. 181–201, Springer, 2010.
- [38] B. K. Kwon, T. R. Oxland, and W. Tetzlaff, “Animal models used in spinal cord regeneration research,” *Spine*, vol. 27, no. 14, pp. 1504–1510, 2002.
- [39] E. C. Clarke, D. F. Fletcher, M. A. Stoodley, and L. E. Bilston, “Computational fluid dynamics modelling of cerebrospinal fluid pressure in chiari malformation and syringomyelia,” *Journal of biomechanics*, vol. 46, no. 11, pp. 1801–1809, 2013.
- [40] S. Cheng, D. Fletcher, S. Hemley, M. Stoodley, and L. Bilston, “Effects of fluid structure interaction in a three dimensional model of the spinal subarachnoid space,” *Journal of biomechanics*, vol. 47, no. 11, pp. 2826–2830, 2014.
- [41] C. Bertram, A. Brodbelt, and M. Stoodley, “The origins of syringomyelia: numerical models of fluid/structure interactions in the spinal cord,” *Journal of biomechanical engineering*, vol. 127, no. 7, pp. 1099–1109, 2005.
- [42] C. Bertram, L. Bilston, and M. Stoodley, “Tensile radial stress in the spinal cord related to arachnoiditis or tethering: a numerical model,” *Medical & biological engineering & computing*, vol. 46, no. 7, pp. 701–707, 2008.
- [43] C. Bertram, “A numerical investigation of waves propagating in the spinal cord and subarachnoid space in the presence of a syrinx,” *Journal of Fluids and Structures*, vol. 25, no. 7, pp. 1189–1205, 2009.

- [44] B. Williams, "On the pathogenesis of syringomyelia: a review.," *Journal of the Royal Society of Medicine*, vol. 73, no. 11, p. 798, 1980.
- [45] B. Williams, "Simultaneous cerebral and spinal fluid pressure recordings," *Acta neurochirurgica*, vol. 59, no. 1-2, pp. 123–142, 1981.
- [46] M. Häckel, V. Beneš, and M. Mohapl, "Simultaneous cerebral and spinal fluid pressure recordings in surgical indications of the chiari malformation without myelodysplasia," *Acta neurochirurgica*, vol. 143, no. 9, pp. 909–918, 2001.
- [47] P. K. Eide, G. Bentsen, A. G. Sorteberg, P. B. Marthinsen, A. Stubhaug, and W. Sorteberg, "A randomized and blinded single-center trial comparing the effect of intracranial pressure and intracranial pressure wave amplitude-guided intensive care management on early clinical state and 12-month outcome in patients with aneurysmal subarachnoid hemorrhage," *Neurosurgery*, vol. 69, no. 5, pp. 1105–1115, 2011.
- [48] P. K. Eide and A. Brean, "Cerebrospinal fluid pulse pressure amplitude during lumbar infusion in idiopathic normal pressure hydrocephalus can predict response to shunting," *Cerebrospinal Fluid Res*, vol. 7, no. 5, 2010.
- [49] P. K. Eide and E. Kerty, "Static and pulsatile intracranial pressure in idiopathic intracranial hypertension," *Clinical neurology and neurosurgery*, vol. 113, no. 2, pp. 123–128, 2011.
- [50] P. K. Eide and W. Sorteberg, "Diagnostic intracranial pressure monitoring and surgical management in idiopathic normal pressure hydrocephalus: A 6-year review of 214 patients," *Neurosurgery*, vol. 66, no. 1, pp. 80–91, 2010.
- [51] R. Frič and P. K. Eide, "Comparison of pulsatile and static pressures within the intracranial and lumbar compartments in patients with chiari malformation type 1: a prospective observational study," *Acta neurochirurgica*, vol. 157, no. 8, pp. 1411–1423, 2015.
- [52] M. Czosnyka and J. D. Pickard, "Monitoring and interpretation of intracranial pressure," *Journal of Neurology, Neurosurgery & Psychiatry*, vol. 75, no. 6, pp. 813–821, 2004.
- [53] B. Williams, "Cerebrospinal fluid pressure changes in response to coughing.," *Brain: a journal of neurology*, vol. 99, no. 2, pp. 331–346, 1976.
- [54] C. A. Sansur, J. D. Heiss, H. L. DeVroom, E. Eskioglu, R. Ennis, and E. H. Oldfield, "Pathophysiology of headache associated with cough in patients with chiari i malformation," *Journal of neurosurgery*, vol. 98, no. 3, pp. 453–458, 2003.
- [55] B. A. Martin, R. Labuda, T. J. Royston, J. N. Oshinski, B. Iskandar, and F. Loth, "Pathological biomechanics of cerebrospinal fluid pressure in syringomyelia: Fluid structure interaction of an in vitro coaxial elastic tube system," pp. 941–942, 2009.